MINDS: water reservoirs of compact planet-forming dust discs: A diversity of H2O distributions

Temmink, M.; Sellek, A.D.; Gasman, D.; Dishoeck, E.F. van; Vlasblom, M.; Pranger, A.; ... ; Tabone, B.

Astronomy & Astrophysics manuscript no. aanda
June 13, 2025

MINDS. Water reservoirs of compact planet-forming dust disks

A diversity of H_2O distributions

Milou Temmink[1], Andrew D. Sellek[1], Danny Gasman[2], Ewine F. van Dishoeck[1,3], Marissa Vlasblom[1], Angèl Pranger[1], Manuel Güdel[4,5], Thomas Henning[6], Pierre-Olivier Lagage[7], Alessio Caratti o Garatti[8,9], Inga Kamp[10], Göran Olofsson[11], Aditya M. Arabhavi[10], Sierra L. Grant[12], Till Kaeufer[13], Nicolas T. Kurtovic[3], Giulia Perotti[14,6], Matthias Samland[6], Kamber Schwarz[6], and Benoît Tabone[15]

(Affiliations can be found after the references)

Received 21/02/2025; accepted 20/05/2025

ABSTRACT

Context. Millimetre-compact dust disks are thought to have efficient radial drift of icy dust pebbles, which has been hypothesised to produce an enhanced cold (T <400 K) H_2O reservoir in their inner disks. Mid-infrared spectral surveys, now with the *James Webb* Space Telescope (JWST), pave the way to explore this hypothesis. In this work, we test this theory for 8 compact disks (R_{dust} <60 au) with JWST-MIRI/MRS observations.

Aims. To explore the H_2O distribution in the inner disk and whether these disks are enhanced in cold H_2O emission, we analyse the different reservoirs that can be probed with the pure rotational lines (>10 μm) by JWST: hot (T > 800 K), intermediate (400< T <800 K), and cold (T <400 K).

Methods. We probe the H_2O reservoirs with JWST-MIRI observations for a sample of 8 compact disks through parametric column density profiles (power laws, jump abundances, and parabolas), multiple component (two or three) slab models, and line flux ratios.

Results. We find that not all compact disks show strong enhancements of the cold H_2O reservoir, instead we propose three different classes of inner disk H_2O distributions. Four of our disks (BP Tau, CY Tau, DR Tau, and RNO 90; Type N or "Normal" disks) appear to have similar H_2O distributions as many of the large and structured disks, as is indicated by the slab model fitting and the line flux ratios. These disks have a small cold reservoir, suggesting the inward drift of dust, but it is not as efficient as hypothesised before. Only two disks (FT Tau and XX Cha; Type E or cold H_2O enhanced disks) do show a strong enhancement of the cold H_2O emission, agreeing with the original hypothesis. The two remaining disks (CX Tau and DN Tau; Type P or H_2O-poor disks) are found to be very H_2O-poor, yet show emission from either the hot or immediate reservoirs (depending on the fit) in addition to emission from the cold one. For the three types, we find that different parametrisations are able to provide a good description of the observed H_2O spectra; a jump abundance at a free temperature is amongst the preferred profiles for all three types, suggesting that this profile can provide a good description of the observed reservoirs for most disks. The multiple component analysis yields similar results as the parametric models. However, in some cases, a power law can give an entirely different distribution compared to the other parametric models. Finally, we also report the detection of other molecules in these disks, including a tentative detection of CH_4 in CY Tau.

Conclusions. Not all compact disks follow the hypothesis that their cold H_2O reservoir is enhanced following efficient radial drift. Therefore, we introduced a classification based on the observed H_2O reservoirs, which should hold for all (isolated) disks: Type N, Type E, and Type P. Type N disks are considered to behave as many other (large and structured) disks, with all three reservoirs present, yet the cold emission is not enhanced. The Type E disks show strong enhancements of the cold H_2O emission, while the Type P disks are generally H_2O-poor.

Key words. astrochemistry - protoplanetary disks - stars: variables: T-Tauri, Herbig Ae/Be - infrared: general

1. Introduction

The inner regions (<10 au) of planet-forming disks are active sites of planet formation (Morbidelli et al. 2012; Dawson & Johnson 2018). The chemical composition of these forming planets is set by the elemental and molecular composition of the nascent disk. One of the key ingredients for habitable worlds is H_2O and, therefore, studying the available H_2O vapour reservoirs in disks is of great importance.

Based on H_2O vapour observations with the *Spitzer* Space Telescope and spatially resolved continuum images with the Atacama Large Millimeter/submillimeter Array, Banzatti et al. (2020) proposed scenarios for the expected H_2O reservoirs given the sizes of the dust disks. Disks that are observed to be compact in their millimetre emission (R_{dust} <60 au) are thought to have efficient radial drift, leading to enriched H_2O reservoirs (N ~10^{18}-10^{21} cm^{-2}) in the innermost regions (< few au) of these disks. The larger, structured disks (60< R_{dust} <300 au) are expected to not show these enriched H_2O abundances (≤$10^{17.5}$ cm^{-2}), since substructures (i.e., gaps and rings) may trap the icy dust grains in the outer regions, halting them from reaching the inner disk and from crossing the H_2O snowline. Furthermore, for disks with large cavities, the situation is expected to be even more extreme, with the inner disks expected to be depleted of H_2O.

Recent modelling works have explored the notion of both unimpeded enhancement due to radial drift and the opposite case of substructures halting the inward drift of pebbles. In particular, Kalyaan et al. (2023) investigated the influence of gaps on the gaseous enhancement in the inner disk. They note that the enhancement, at least for the H_2O vapour reservoir, is of limited duration (up to a few million years), before the material gets accreted onto the host star. Only when the gaps do not block the dust entirely, but some of the grains are still able to pass through (Pinilla et al. 2024; Mah et al. 2024), the lifetime of this enhanced reservoir can be prolonged. However, the inward drift of the dust particles does not only enhance the gaseous reservoir,

Table 1: Stellar properties and observational details of the sample of compact disks studied in this work.

Source	M_*	L_*	Dist.	v_{hel}	Inclination	R_{in}	$R_{dust,95\%}$	Obs. date	Int. time	References
	[$M_\odot$]	[$L_\odot$]	[pc]	[km s^{-1}]	[°]	[au]	[au]	dd/mm/yyyy	[min]	$M_*/L_*/v_{hel}/i/R_{dust}$
BP Tau	0.52	0.40	129	16.76	23.6	0.04	41	20/02/2023	29.0	$m1, l1, v1, i1, d1$
CX Tau	0.37	0.26	128	19.30	55.1	0.04	38	20/02/2023	60.0	$m2, l2, v2, i2, d2$
CY Tau	0.31	0.26	128	15.10	32.0	0.04	<64	20/02/2023	60.0	$m2, l2, v2, i3, d3$
DN Tau	0.52	0.70	128	18.80	35.2	0.06	61	28/09/2023	60.0	$m1, l1, v2, i4, d1$
DR Tau	0.93	0.63	195	27.60	5.4	0.06	54	04/03/2023	27.8	$m1, l1, v3, i4, d1$
FT Tau	0.34	0.15	127	17.24	35.5	0.03	45	20/02/2023	30.0	$m1, l1, v4, i4, d1$
RNO 90	1.50	2.14	117	-10.10	37.0	0.10	<47	25/08/2023	33.4	$m3, l3, v5, i5, d3$
XX Cha	0.36	0.29	190	16.26	39.7	0.04	<25	31/08/2023	60.0	$m4, l4, v6, i6, d3$

Notes. All distances have been acquired from GAIA (Gaia Collaboration et al. 2018). References (mass, luminosity, heliocentric velocity, inclination, dust radii): $m1$-Long et al. (2019), $m2$-Simon et al. (2017), $m3$-Banzatti et al. (2022), $m4$-Manara et al. (2016), $l1$-Long et al. (2019), $l2$-Herczeg & Hillenbrand (2014), $l3$-Banzatti et al. (2022), $l4$-Manara et al. (2016), $v1$-Fang et al. (2018), $v2$-Banzatti et al. (2019), $v3$-Ardila et al. (2002), $v4$-Roccatagliata et al. (2020), $v5$-Banzatti et al. (2022), $v6$-Nguyen et al. (2012), $i1$-Gasman et al. (2025), $i2$-Facchini et al. (2017), $i3$-Simon et al. (2017), $i4$-Long et al. (2019), $i5$-Bosman & Bergin (2021), $i6$-This work, $d1$-Long et al. (2019), $d2$-Facchini et al. (2019), $d3$-Estimated in this work

it also increases the opacity of the dust itself. Recent models by Sellek et al. (2025) suggest that the increased opacity of the dust elevates the τ=1 layer of the continuum and, therefore, may hide a larger gas reservoir that lies deeper in the disk. The observable column densities may thus not reflect the enhanced reservoirs. Further work by Houge et al. (2025) supports this idea and also investigated the competition between photodissociation and vertical mixing on the available reservoir. Finally, Kalyaan et al. (2023), Sellek et al. (2025), and Easterwood et al. (2024) note the importance of the gap locations and the time at which they form for the drifting pebbles. Gaps located at smaller radial distances and which formed early on are more effective at limiting the gaseous enhancement, as more dust grains are blocked outside the snowline. However, they may leak more for a given gap depth or grain size. For gaps located at larger radial distances, the enhancement is stronger, as a smaller icy dust reservoir is blocked. Furthermore, the way the gap opens may also be of importance. Lienert et al. (2024) have shown that gaps opened due to internal photoevaporation are able to block both the pebble and gas flow, strongly influencing the inner disk composition. In contrast, models by Greenwood et al. (2019) have shown that, in the absence of gaps, the dust opacity decreases as the disk evolves with time and this leads to an increase in the H_2O flux. Current observations of mid-infrared spectra of large and structured disks with the *James Webb* Space Telescope (JWST), including those with large cavities, already show that inner regions of such disks are not completely void of H_2O (Perotti et al. 2023; Schwarz et al. 2024) and, in some cases, they may have strong emission from the cold reservoir (<400 K; Gasman et al. 2023, 2025).

The *James Webb* Space Telescope (Rigby et al. 2023) provides the best opportunity to fully explore the available H_2O reservoirs in the inner regions of planet-forming disks, using the increased sensitivity and resolution of the Medium Resolution Spectrometer (MRS; Wells et al. 2015; Argyriou et al. 2023) of the Mid-InfraRed Instrument (MIRI; Wright et al. 2015; Rieke et al. 2015; Wright et al. 2023) with respect to the *Spitzer* Space Telescope. Since its launch, multiple works have studied the available reservoirs, including the analysis of H_2O emission across the entire JWST-MIRI wavelength range (Gasman et al. 2023) using 0D local thermal equilibrium (LTE) slab models. This analysis directly proved the existence of an expected radial temperature gradient, where the longer wavelengths probe larger radii and, thus, colder temperatures (Blevins et al. 2016; Banzatti et al. 2017, 2023b, 2025). Banzatti et al. (2023a) identified the emergence of a cold H_2O reservoir (T <240 K), which is expected to be the effect of radial dust drift. Subsequently, multiple slab models were fitted to the pure rotational H_2O spectra (> 10 μm) identifying the available reservoirs (Pontoppidan et al. 2024; Temmink et al. 2024a), and a third cold component, in addition to hot (>800 K) and warm (400 < T < 800 K components, was found to be necessary to describe the same cold H_2O reservoir of T <240 K. The three-component analysis of Temmink et al. (2024a) also provided another confirmation of the radial temperature gradient, where the multiple component analysis of DR Tau could be approximated with a temperature profile of $T(R) \sim 500\,(R/1\mathrm{au})^{-0.5}$ K. More recently, efforts have been made to increase the complexity by moving away from using multiple components and to describe the temperature and column density profiles by parametric functions (Kaeufer et al. 2024; Romero-Mirza et al. 2024). These profiles, including simple and exponentially tapered power laws, show that the pure rotational H_2O transitions can be explained by such parametric models, but this has only been tested for a limited sample of disks with different disk characteristics, such as their radial sizes and structures. We also note the effort by Woitke et al. (2024), who, for the first time, used a full 2D thermochemical code to model the observed molecular emission in the outbursting source of EX Lup.

In this work, we aim to analyse the pure rotational H_2O emission in 8 millimetre-compact disks (dust radii of $R_{dust,95\%} \sim 25 - 60$ au; Long et al. 2019; Facchini et al. 2019), using both the parametric and multiple component techniques highlighted above. Our criterion for a dust disk to be compact follows the classification of Banzatti et al. (2020), i.e., compact disks have dust radii $\lesssim$60 au. All sources have been observed with JWST/MIRI-MRS as part of the JWST Guaranteed Time Observations Program MIRI mid-INfrared Disk Survey (MINDS, PID:1282, PI: T. Henning; Kamp et al. 2023; Henning et al. 2024). Throughout our analysis, we aim to investigate the strengths of the different H_2O reservoirs, indicated throughout the paper as hot (>800 K), intermediate (400-800 K), and cold (<400 K, see also Banzatti et al. 2023a). We use this to explore the H_2O reservoirs and column density profiles. In addition, we also infer whether these compact disks show an enhancement in the cold H_2O reservoir, as suggested by Banzatti et al. (2020), or whether the situation is more complex than this scenario.

The paper is structured as follows: Section 2 describes the

sample and the observations, while Section 3 contains a description of the used methodology. The results are represented in Section 4, and are interpreted in Section 5. Aside from the interpretation, Section 5 also discusses the role of substructures in setting the H_2O reservoirs and makes a comparison with existing models. Finally, Section 6 contains our conclusions and a short summary.

2. Sample and observations

2.1. Sample

Our sample of compact planet-forming disks consists of eight sources: BP Tau, CX Tau, CY Tau, DN Tau, DR Tau, FT Tau, RNO 90, and XX Cha, for which stellar properties are summarised in Table 1. Dedicated papers, exploring the observed molecular emission, exist for two of the sources: CX Tau (Vlasblom et al. 2025) and DR Tau (Temmink et al. 2024b,a).

Although the disks in our sample are known to be rather compact in the millimetre continuum emission ($R_{\rm dust}$ $\lesssim$60 au), limited information is known about their gas disk sizes ($R_{\rm gas}$). Trapman et al. (2019) proposed that a gas-to-dust size ratio of $R_{\rm gas}/R_{\rm dust}$ >4 is a clear sign of radial drift. For our sources, only one disk has literature values for both $R_{\rm dust}$ and $R_{\rm gas}$: CX Tau (Facchini et al. 2019). These values suggest a ratio of $R_{\rm gas}/R_{\rm dust}$ >5, hinting at strong radial drift being the potential cause of this disk's compactness. For the other disks, the gas radius has not been determined and, in some cases, high-resolutions observations of the continuum emission do not (yet) exist. Consequently, the gas-to-dust size ratio is still to be determined in a consistent manner and it is unclear whether the compactness of these disks can be attributed to an evolution dominated by radial drift or simply to their initial conditions. For these reasons, we have chosen our sample to follow the criteria of Banzatti et al. (2020) and consider the disks with millimetre continuum emission radii of $R_{\rm dust}$ $\lesssim$60 au to be compact.

As can be seen from Table 1, our sample is rather homogeneous in terms of masses, luminosities, and inclinations. There are a few outliers: i.e., DR Tau and RNO 90 have higher stellar masses compared to the others, while DR Tau also has the lowest inclination (i ~5.4°, Long et al. 2019). CX Tau, on the other hand, has the highest inclination (~55.1°). Furthermore, as 6 out of 8 disks are located in the Taurus star-forming region, we can expect them to be of similar ages (~1-3 Myr, Krolikowski et al. 2021; Luhman 2023). In contrast, RNO 90 is located in Ophiuchus and may, therefore, be on the younger side. These small differences suggest that our sample is overall rather homogeneous and differences must therefore be due to either their initial conditions or differences in their (potentially drift-dominated) evolution. A larger sample will be analysed in Temmink et al. (in prep.), which may provide more insights into the differences related to the stellar properties.

2.2. Observations and data reduction

The JWST-MIRI/MRS details (date of observation and integration time) are also included in Table 1. All MRS spectra have been taken in the FASTR1 readout mode with a four-point dither pattern using all three grating settings (A, B, and C). All data have been reduced using a standard pipeline reduction (version 1.16.1; Bushouse et al. 2024) and pmap 1315. The spectra have been extracted through aperture photometry, where the aperture has a size of 2× the full width at half maximum (FWHM). Additionally, we have corrected for residual fringes using the implementation of the default pipeline, as most of the observations (except XX Cha) were taken without target acquisition. The resulting spectra were continuum subtracted using an updated version of the method by Temmink et al. (2024b), which makes use of the 'Iterative Reweighted Spline Quantile Regression' method included in the PYBASELINES package (Erb 2022). Before estimating the continuum, downward spikes were masked using the same method as in Temmink et al. (2024b), but now they were masked per MIRI subband as opposed to over the whole spectrum. We used a quantile regression value of 0.1 and placed the knots of the cubic splines every 75 data points, except for Channel 4 and the silicate feature (~8.25-11.25 μm), where the knots were placed every 25 points to better estimate the varying continuum. For CX Tau and DN Tau, a knot spacing of 25 data points was used for the entire spectrum, due to their strongly varying continuum. Given the large uncertainty of the observations at the location of the silicate feature, the quantile regression value was set to 0.5 for all disks, which places the baseline through the median of the observations. Additionally, we changed the continuum estimate for the Q-branches of CO_2, HCN, and C_2H_2. The typical fit could overestimate the continuum of these Q-branches, effectively taking away molecular flux in the subtraction. To avoid this oversubtraction, we used a cubic interpolation of the estimated baseline just before and after the Q-branch to better fit the continuum level underneath the Q-branch. In particular, we masked the 13.45-14.20 μm wavelength region that captures the HCN and C_2H_2 Q-branches, and the 14.88-15.01 μm region for that of CO_2. The reduced spectra and continuum estimates are displayed in Figure 1.

Figure 1 shows that the shape of the spectra overall look similar and in some cases nearly indistinguishable. All sources have a silicate feature at ~10 μm and contain emission features from a variety of molecular species. The only outlier is CY Tau, which has stronger emission at the shortest wavelengths. This is very likely due to an inner (puffy) rim self-shadowing the outer disk and, subsequently, lowering the mid- and far-infrared flux (see, for example, Dullemond & Dominik 2004; Woitke et al. 2019). We leave the analysis of the dust continua for future work.

3. Methodology

To analyse the pure rotational H_2O emission in the JWST-MIRI/MRS spectra of our sample of compact disks, we use slab models under the assumption of local thermal equilibrium (see Grant et al. 2023; Tabone et al. 2023 for more details on the slab model generation). Following Banzatti et al. (2025), we include mutual line shielding in the H_2O slab models to account for the shielding of ortho- and para-line pairs. Additionally, we take the mean spectral resolution, calculated using the results of Pontoppidan et al. (2024) and the updates by Banzatti et al. (2025), of each MIRI subband to properly sample the wavelength grid of the slabs over the entire spectrum. We use two different line widths for our models: a constant value of ΔV=4.71 km s^{-1}, which is the line width of H_2 at a temperature of 700 K (Salyk et al. 2011), as well as a similar approach to Romero-Mirza et al. (2024), where the line width is taken as the sum in quadrature (hereafter simply called the quadrature line width) of the turbulent line width ($\Delta V_{\rm turb}$ fixed to 1.0 km s^{-1}) and the thermal line width ($\Delta V_{\rm therm} = \sqrt{2kT/m}$, with T the temperature of the slab model and m the mass of an H_2O molecule). The two line widths are used to make a comparison between the practices used in the recent literature. While the earlier works (e.g., Tabone et al. 2023; Grant et al. 2023; Gasman et al. 2023) have used a constant value of 4.71 km s^{-1}, Romero-Mirza et al. (2024) recently

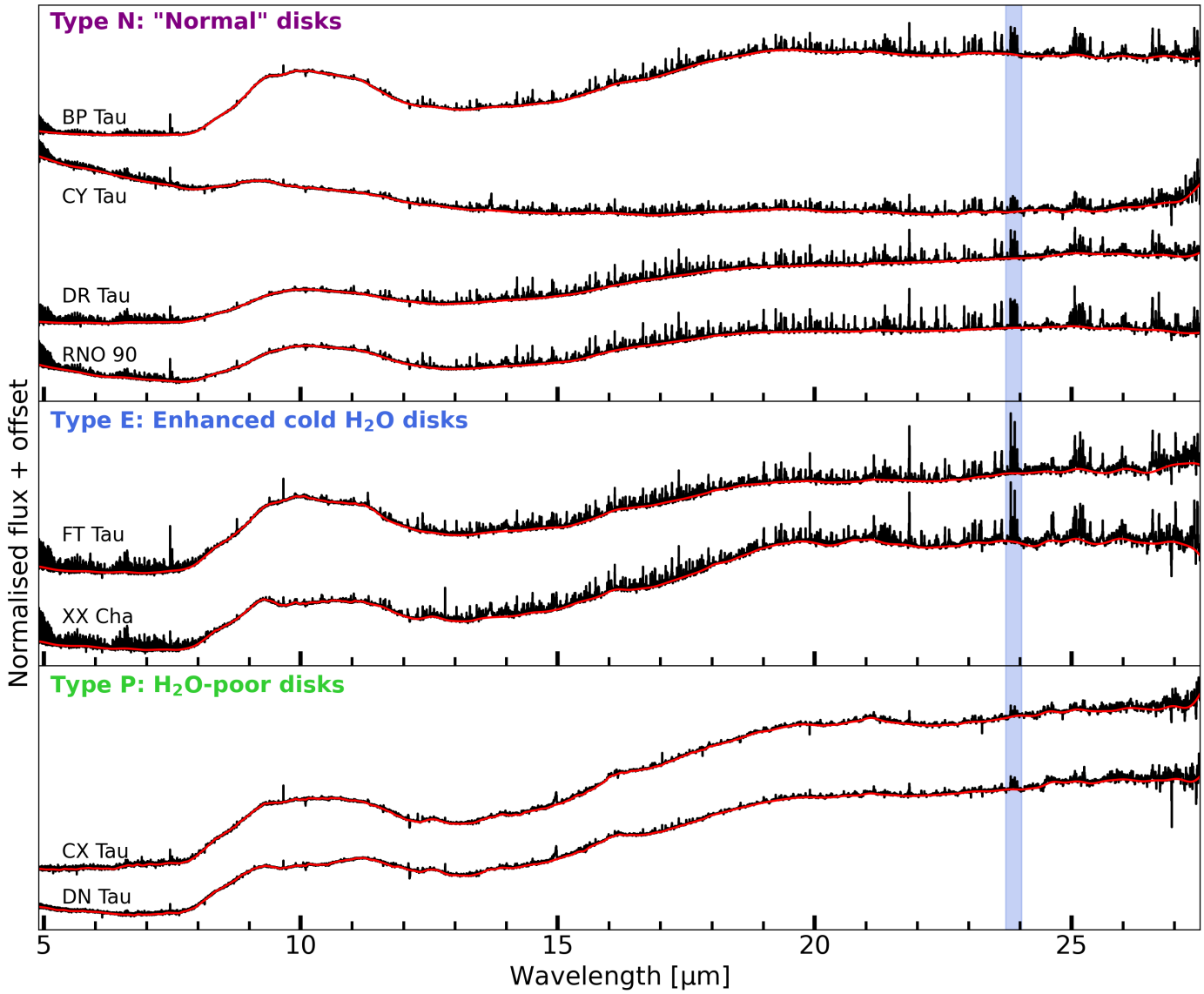

Fig. 1: Normalised to peak flux spectra of our sample of millimetre-compact disks. The red line indicates the estimated continuum. The indicated types and their meaning are discussed in Section 5.1. In blue we have highlighted the 23.72-24.03 μm wavelength region, where two transitions are located that are most important for obtaining information about the cold H_2O reservoir.

used the sum in quadrature. To investigate which one of these approaches fits better to our spectra, we test both options in our fits and make a comparison in Section 5.4. The python-package SPECTRES (Carnall 2017) is subsequently used to resample the slab models onto the wavelength grid of MIRI. However, before resampling, we apply a wavelength shift to the slab models (see also Pontoppidan et al. 2024), based on the heliocentric velocity of the sources (see Table 1). Figure A.1, using the spectrum of DR Tau as an example, shows that these wavelength shifts, although subtle, are required to properly recreate the observed line profiles and, subsequently, will improve fit results.

We fit our spectra using two different approaches: similar to Temmink et al. (2024a), we use a multi-component analysis where three or two distinct components (with decreasing temperatures and increasing emitting areas) are fitted to the entire rotational spectrum. Furthermore, we use and extend upon the methods implemented by Romero-Mirza et al. (2024), who used (exponentially-tapered) power law profiles for the temperature and column density. We denote these models as multi-component and parametric models, where in the latter case we explore more options than (exponentially tapered) power laws. By using both these methods, we can explore the strengths of the different H_2O reservoirs and investigate the robustness of what kind of profile for the column density is preferred in the inner region. By using both techniques, we also gain more insights into the changing excitation conditions with radius in the inner regions of these disks.

3.1. Rotational H_2O spectrum: parametric analysis

In an attempt to parametrically describe the observed H_2O emission, we follow the approach by Romero-Mirza et al. (2024): 50 slab models are used to sample profiles in both temperature and column density as a function of the emitting radius. As opposed to Romero-Mirza et al. (2024), we first determine the radius as a

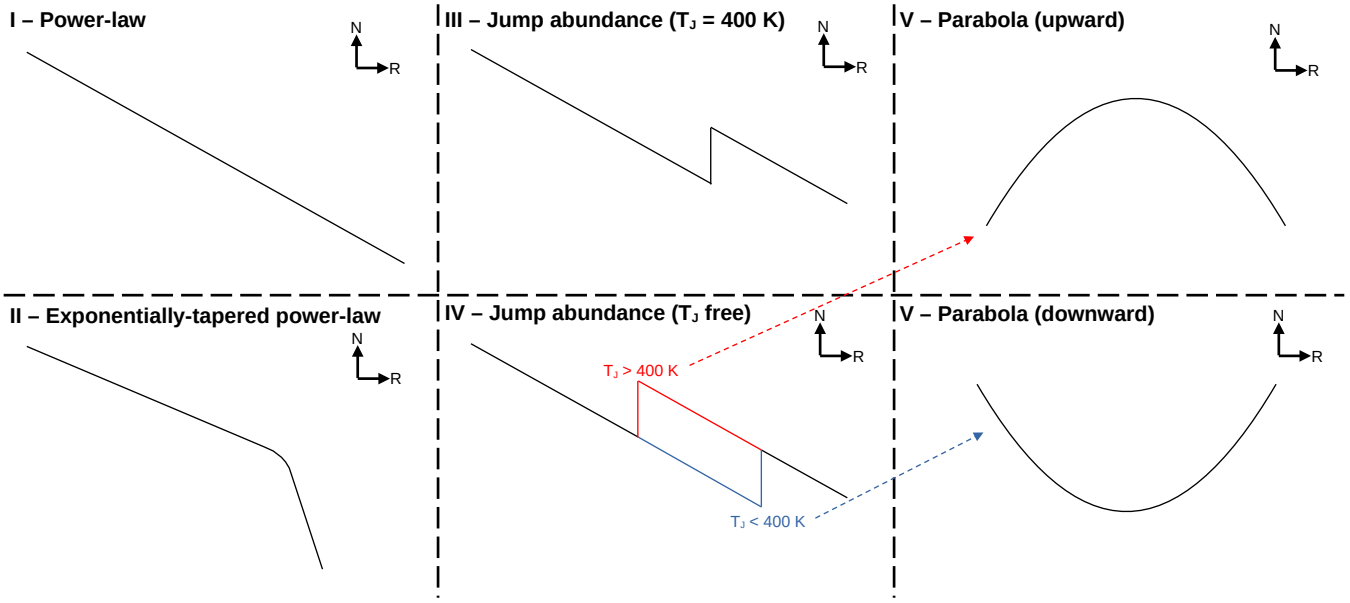

Fig. 2: Schematic highlighting the different parametric models used for the column density profiles. Both the horizontal (radius) and vertical (column density) axes are taken in $\log_{10}$-space.

function of temperature,

$$R(T) = R_{\rm in}\left(\frac{T}{1500\ {\rm K}}\right)^{-1/q}. \quad (1)$$

This relation ensures that the inner radius ($R_{\rm in}$ (in au), as listed in Table 1) of our slab models is located at the estimated dust sublimation radius at 1500 K. Using this equation, we sample the annular emitting regions of our 50 slab models for temperatures between 1500 K (the dust sublimation radius; Barvainis 1987) and 150 K (the condensation temperature of H_2O; Collings et al. 2004) in $\log_{10}$-space. The dust sublimation radius has been calculated following the approach of Dullemond et al. (2001), $R_{\rm in} \sim 0.07\sqrt{(L_*/L_\odot)}$. Both the calculated inner radii and adopted stellar luminosities can be found in Table 1. By simply rewriting Equation 1 we obtain a relation for the temperature as a function of the radius,

$$T(R) = 1500\ {\rm K}\left(\frac{R}{R_{\rm in}}\right)^{-q}. \quad (2)$$

For the column density, we use the same profiles as Romero-Mirza et al. (2024): a power law (profile I, Equation 3) and an exponentially tapered power law (profile II, Equation 4). In addition, we also try different profiles. Figure 2 provides a schematic overview of the different profiles and their potential behaviours. In particular, we assume a constant number of molecules ($\mathcal{N}_{\rm mol}$) with radius, that is each annulus contains the same number of molecules, which automatically resembles a power law with a power of -2 (the emitting area, A, is proportional to the square of the radius). We then allow this number of molecules to experience a jump, i.e., the number of molecules gets enhanced (or depleted) by a factor $F_{\rm scale}$, at temperatures below a given jump temperature, $T_{\rm jump}$ (see Equation 5). We have tried profiles with a fixed jump temperature, at 400 K (profile III), and we have kept $T_{\rm jump}$ as a free parameter (profile IV). The value of 400 K resembles approximately the boundary temperature between the sublimated (colder temperatures) and gas-phase formed (hotter temperatures) H_2O vapour reservoirs (see also Romero-Mirza et al. 2024). The jump temperature can move to higher temperatures, indicating a potential depletion of the hot H_2O reservoir, or to colder temperatures, representing a potential enhancement of the cold H_2O reservoirs. A parabola provides a smoother description of this behaviour: the jump moving to higher temperatures is captured by an upward parabola (the parabola has a maximum), while a downward parabola (the parabola has a minimum) captures the behaviour of the jump moving to lower temperatures (see also Figure 2). Therefore, we fitted a parabola in log space (profile V, Equation 6). The equations describing the column density profiles of each of these cases are:

$$N_{\rm I}(R) = N_0\left(\frac{R}{1{\rm au}}\right)^{-p}. \quad (3)$$

$$N_{\rm II}(R) = N_0\left(\frac{R}{1{\rm au}}\right)^{-p}\exp\left[-\left(\frac{R}{R_{\rm c}}\right)^{\phi}\right]. \quad (4)$$

$$N_{\rm III,IV}(R) \propto \begin{cases} \frac{\mathcal{N}_{\rm mol}}{A} & \text{if } T > T_{\rm jump}. \\ \frac{\mathcal{N}_{\rm mol}\times F_{\rm scale}}{A} & \text{if } T \leq T_{\rm jump}. \end{cases} \quad (5)$$

$$N_{\rm V}(R) = N_0\left(\frac{R}{1{\rm au}}\right)^{\alpha+\beta\ln(R/1{\rm au})}. \quad (6)$$

The emitting area of each slab model is accounted for in the exact same manner as reported in Romero-Mirza et al. (2024). The area is multiplied by the cosine of the disk's inclination (i, reported in Table 1), $A = \pi\left(R_2^2 - R_1^2\right)\times\cos(i)$, where R_1 and R_2 are, respectively, the inner and outer radii of each annulus (see also Equation 1).

We fit the profiles, sampled by the 50 slab models, using a Markov Chain Monte Carlo (MCMC) approach, implemented through the EMCEE python-package (Foreman-Mackey et al. 2013). From the posterior distribution of the MCMC, we take the median values as the best-fit values for the fitted parameter. Additionally, the 18$^{\rm th}$ and 84$^{\rm th}$ percentiles are taken as the lower and upper 1σ uncertainties. We use a reduced-χ^2 as the likelihood function of the MCMC, in order to compare the full

model (the sum of the 50 slab models) with the observations. The likelihood has, therefore, the following form:

$$\chi^2_{\rm red} = \frac{1}{N_{\rm data}} \sum_i \frac{w_i \left(F_{{\rm obs},i} - F_{{\rm model},i}\right)^2}{\sigma_i^2}, \quad (7)$$

where $F_{\rm obs}$ is the observed spectrum and $N_{\rm data}$ is the number of data points within the used fit regions. σ denotes the noise of the observations, determined in a similar manner as in Temmink et al. (2024b), where the *James Webb Exposure Time Calculator*[1] has been used to obtain the continuum signal-to-noise (S/N) at the midpoint of each subband given the observational setup. The values for the S/N-ratios are given in Table B.1. As the noise is significantly higher in Channel 4 and many important H_2O lines can be found at these wavelengths, we slightly offset the large noise by introducing weights in the χ^2-formula, w_i. All fit regions beyond 20 μm have been given a higher weight of 5, while select regions with important transitions probing the cold reservoir have been given a weight of 10 or 15 (for the strongest transitions). While the values are arbitrary, these weights ensure that we are able to properly fit the full rotational spectrum, without favouring the hot reservoir as the transitions at smaller wavelengths have lower flux uncertainties. Fits without any weights favour the hot reservoir. Therefore, the chosen weights ensure that our models properly fit all reservoirs, including the cold one that is best probed by the longer wavelengths that are more noisy given the lower sensitivity of JWST/MIRI's Channel 4. While the choice for the weights is arbitrary, using lower weights will still favour the hotter reservoirs and result in a worse fit for the colder reservoir, whereas higher weights may start overrepresenting the cold reservoir and result in worse fits for the hot one.

In the MCMC, we use 20 walkers per free parameter and allow the MCMC to explore the prior space for 50,000 iterations. Table 2 lists the prior spaces for each profile. Common priors that are kept the same in each fit are only listed once, for example, the number of molecules, $\mathcal{N}_{\rm mol}$, in the jump abundances. For some sources, we run a second fit with a more limited prior space. In these cases, a second, less favourable solution was often found and a number of walkers got stuck in this local minimum, not allowing the fit to converge. The updated prior space was subsequently chosen to exclude these local minima. All fits use selected isolated H_2O lines and ortho-para line pairs, which all have been taken from Banzatti et al. (2025) (see their Figure 3 and Tables 5 and 6). The used fit regions, which are also shifted by the heliocentric velocity, are listed in Table C.1. We have used fewer regions for CX Tau and DN Tau as the CO_2 *P*- and *R*- branches strongly contribute to their observed emission.

3.2. Rotational H_2O spectrum: multiple components

As a comparison, we also follow Temmink et al. (2024a) to investigate the pure rotational H_2O spectrum using two (in the case of CX Tau and DN Tau) or three slab model components. Through trial and error (i.e., by fitting three or two components), we found that only two components were needed to fully describe the rotational H_2O spectra of CX Tau and DN Tau. This is very likely due to the H_2O emission being much weaker compared to the other sources (see Figure 1). We do not use all three approaches presented in Temmink et al. (2024a), but only the simplest one, Approach I, which assumes a simple radial gradient. The line optical depths are sufficiently high that the vertical gradient in Approach III does not matter and the results resemble that of Approach I.

[1] Exposure Time Calculator: https://jwst.etc.stsci.edu/

Table 2: Priors used for the profiles listed in Section 3.1.

Profile	Parameter	Priors
Temperature-radius	q	$\mathcal{U}(0, 5)$
Power law (I)	$\log_{10}(N_0)$	$\mathcal{U}(12, 30)$
	p	$\mathcal{U}(-10, 10)$
Exponential taper (II)	$\log_{10}(R_c)$	$\mathcal{U}(\log_{10}(R_{\rm in}), 1)$
	ϕ	$\mathcal{U}(0.5, 5)$
Jump abundance (III)	$\log_{10}(\mathcal{N}_{\rm mol})$	$\mathcal{U}(30, 50)$
	$\log_{10}(F_{\rm scale})$	$\mathcal{U}(-3, 5)$
Free temperature (IV)	$T_{\rm jump}$	$\mathcal{U}(150, 1500)$
Parabola (V)	$\log_{10}(N_0)$	$\mathcal{U}(12, 30)$
	α	$\mathcal{U}(-100, 100)$
	β	$\mathcal{U}(-50, 50)$

To agree with the parametric analyses discussed in Section 3.1, we slightly adapt Approach I: instead of having a circular area surrounded by two annuli, we use three annuli with the inner radius of the first set to the dust sublimation radius, $R_{\rm in}$. The other two or three radii are kept free, together with their respective temperatures and column densities. Therefore, Equation 2 of Temmink et al. (2024a) becomes:

$$\begin{aligned} F_{\rm total} = {} & F_1 \pi \left[\left(\frac{R_1}{1\,{\rm au}}\right)^2 - \left(\frac{R_{\rm in}}{1\,{\rm au}}\right)^2 \right] \cos(i) \\ & + F_2 \pi \left[\left(\frac{R_2}{1\,{\rm au}}\right)^2 - \left(\frac{R_1}{1\,{\rm au}}\right)^2 \right] \cos(i) \\ & + F_3 \pi \left[\left(\frac{R_3}{1\,{\rm au}}\right)^2 - \left(\frac{R_2}{1\,{\rm au}}\right)^2 \right] \cos(i) \end{aligned} \quad (8)$$

For the sources for which we only fit two components, the third term in the above equation can be ignored.

The fits are made using the same MCMC setup, with the same reduced-χ^2 formula taken as the likelihood (see Equation 7), as in Section 3.1. The same fit regions are used for the most optimal comparison between the results.

3.3. Line flux ratios

Aside from analysing the spectrum through slab models, we follow Banzatti et al. (2025) and analyse their suggested line flux ratios: $F_{1500{\rm K}/3600{\rm K}}$ and $F_{3600{\rm K}/6000{\rm K}}$ (see also the rightmost panel in their Figure 10). In particular, these line ratios will provide information on, respectively, the cold and hot H_2O vapour reservoirs. The temperatures indicate the approximate upper level energy. The 1500 K flux is comprised of two isolated H_2O transitions, with upper level energies of, respectively, 1448 K (at λ=23.81676 μm) and 1615 K (at λ=23.89518 μm), while the 3600 K and 6000 K fluxes are taken to be the isolated lines at 17.50436 μm and 17.32395 μm. Given their upper level energies, these lines probe the strength of the different temperature reservoirs and the ratios provide insights into the potential enhancement of the cold reservoir. Following Banzatti et al. (2025), we take the sum from the line fluxes of the 1448 K and 1615 K transitions as the total value for $F_{1500{\rm K}}$. To determine the line fluxes, we followed the approach of Banzatti et al. (2012) and Temmink et al. (2024b), based on the techniques provided by Pascucci et al. (2008), Najita et al. (2010), and Pontoppidan et al. (2010): we obtained a Gaussian distribution of measured line flux, using 1000 iterations of adding normally distributed noise (following the S/N-ratios in Table B.1), by fitting Gaussians (us-

ing the python-package LMFIT, Newville et al. 2024) to the lines. From these distributions, we take the median value as the line flux and the full width at half maximum (FWHM) as the uncertainty.

4. Results

In the following section, we highlight the results from our different fitting methods. In Section 4.1, we present the parametric results for the different fit profiles, while the results of the multiple component analysis are shown in Section 4.2. The calculated line fluxes for the different line tracers are displayed in Section 4.3.

4.1. Parametric analysis

Figure 3 displays all fitted profiles for our sample of compact disks with a line width of 4.71 km s^{-1}. Those for the quadrature line widths are given in Figure D.1. Given the profiles, we find three groups of disks: BP Tau, CY Tau, DR Tau, and RNO 90 all behave very similarly, which is most notable in the exponentially tapered power laws (second column), the jump abundances with $T_{\rm jump}$ at higher temperatures ($T_{\rm jump} \gtrsim 650$ K, fourth column), and the resulting upward parabolas (fifth column). The resulting profiles for FT Tau and XX Cha are also nearly identical, but differ from the other four sources. The jump abundance occurs at a low temperature of $T_{\rm jump} \leq$250 K for these disks, while their power laws are very slowly declining and their downward parabolas are very shallow. Finally, aside from their very similar spectra (see Figure 1), the parametrisations of CX Tau and DN Tau also behave very similarly to each other, but different from the other disks. Their jump abundance occurs at the intermediate temperatures $T_{\rm jump}$ ~500-600 K, while their power laws are monotonically increasing with radius and their parabolas are turned downwards.

The $\chi^2_{\rm red}$ values are listed in Table D.1, where we have highlighted the parametrisation with the lowest $\chi^2_{\rm red}$-value in bold face. Figures D.2-D.9 compare these best-fitting models with the observations and the fitting parameters are also listed in Tables D.2 and D.3. These tables also include uncertainty values on the retrieved fitting parameters. Those uncertainties are taken as the 16$^{\rm th}$ and 84$^{\rm th}$ percentiles of the posterior distributions and, therefore, represent the 1σ upper and lower limits, respectively. From the $\chi^2_{\rm red}$ values, it is clear that not one single parametrisation provides the best description of all observations. Instead, a combination of the different profiles is preferred. We also note that the $\chi^2_{\rm red}$ values of the different parametrisations are overall very similar.

Finally, we briefly highlight the resulting temperature slopes (values for q, see Equations 1 and 2) according to our retrieved profiles. From Tables D.2 and D.3 it is clear that our retrieved values of q are between 0.35 and 1.30. Overall, we find the lower values for BP Tau, DR Tau, FT Tau, RNO 90, and XX Cha, while the higher values are found for CX Tau, CY Tau, and DN Tau. The average of the best-fitting parametrisations for all disks suggest a power law slope of q ~0.57 for the temperature, which is somewhat lower than the value found by Romero-Mirza et al. (2024) of q ~0.69 and the value suggested by thermochemical modelling of q ~0.7 in the surface layers of disks (Bosman et al. 2022, Vlasblom et al. in prep.). Our average value would be even lower if we had only accounted for the results from the quadrature line widths.

4.2. Multiple component analysis

Overall, we find rather good agreement between the best-fitting profiles and the multiple components (3 or 2), as can be seen in Figures 3 and D.1, where the discrete data points indicate the results of such fits. The resulting values are given in Table D.4, while the $\chi^2_{\rm red}$ values are also listed in Table D.1. We note that the radial locations shown in Figures 3 and D.1 are not the values for R_1, R_2, and R_3, the outer edge of each emitting area, but these are the central values of each emitting area. The resulting spectra for the best-fitting models are also included in Figures D.2-D.9 (red profiles).

The results for the multiple component analysis are rather similar between the different disks with either 3 or 2 component fitted: for the 3 component fits, we find that the temperatures for the first component all fall in the 765-970 K range, while those for the second and third components fall in the respective ranges of 355-530 K and 200-300 K. We note that the temperatures of the second and third components for FT Tau and XX Cha (T_2 ~385 and T_3 <215) are lower than those for BP Tau, CY Tau, DR Tau, and RNO 90, further suggesting a difference in behaviour as seen for the parametric analysis in Section 4.1. The temperatures for CX Tau and DN Tau, where only two components were fitted, are also very similar. The first component has a temperature between ~400-500 K for both sources with slightly higher temperatures for DN Tau, while the second component has a temperature in the range of 190-240 K.

Similarly, the column densities follow the same structure, where generally the first component has the highest column density, followed by the second and the third (where applicable). We note, however, that the retrieved column densities cannot be assumed to lie on a simple power law: as can be seen in Figure 3 and D.1 the other parametrisations provide better agreement with the multiple component fits. For example, the downward parabola structure of CX Tau and DN Tau cannot be captured by a power law through the individual components. Finally, the high values for the emitting areas of the third component very likely indicate optically thin emission (see also Temmink et al. 2024a).

4.3. Line flux ratios

The values for the derived line fluxes are given in Table F.1, while the ratios are displayed in Figure 4, which has been adapted from Banzatti et al. (2025) (see their Figure 10, right panel) to include our sample of compact disks (the coloured data points). The grey data points are those from Banzatti et al. (2025), using the values listed in their Table 3. We find that BP Tau, CY Tau, DR Tau, and RNO 90 show similar line flux ratios as the sample of Banzatti et al. (2025), while the line fluxes of the cold lines ($F_{1500\ \rm K}$) are much stronger in FT Tau and XX Cha. CX Tau and DN Tau also appear to have higher cold line fluxes, but we note that their hot H_2O line fluxes ($F_{6000\rm K}$) are significantly lower. The implications of the locations of the different disks in Figure 4 are further discussed in Section 5.1.

5. Discussion

In the following sections, we discuss and interpret our results. From our analysis, it immediately becomes clear that these disks, even though they are all classified as compact, show different behaviours given their H_2O spectra and inferred H_2O distributions. Not all of these disks show a strong enhanced cold H_2O reservoir, suggesting that additional factors are at play within these

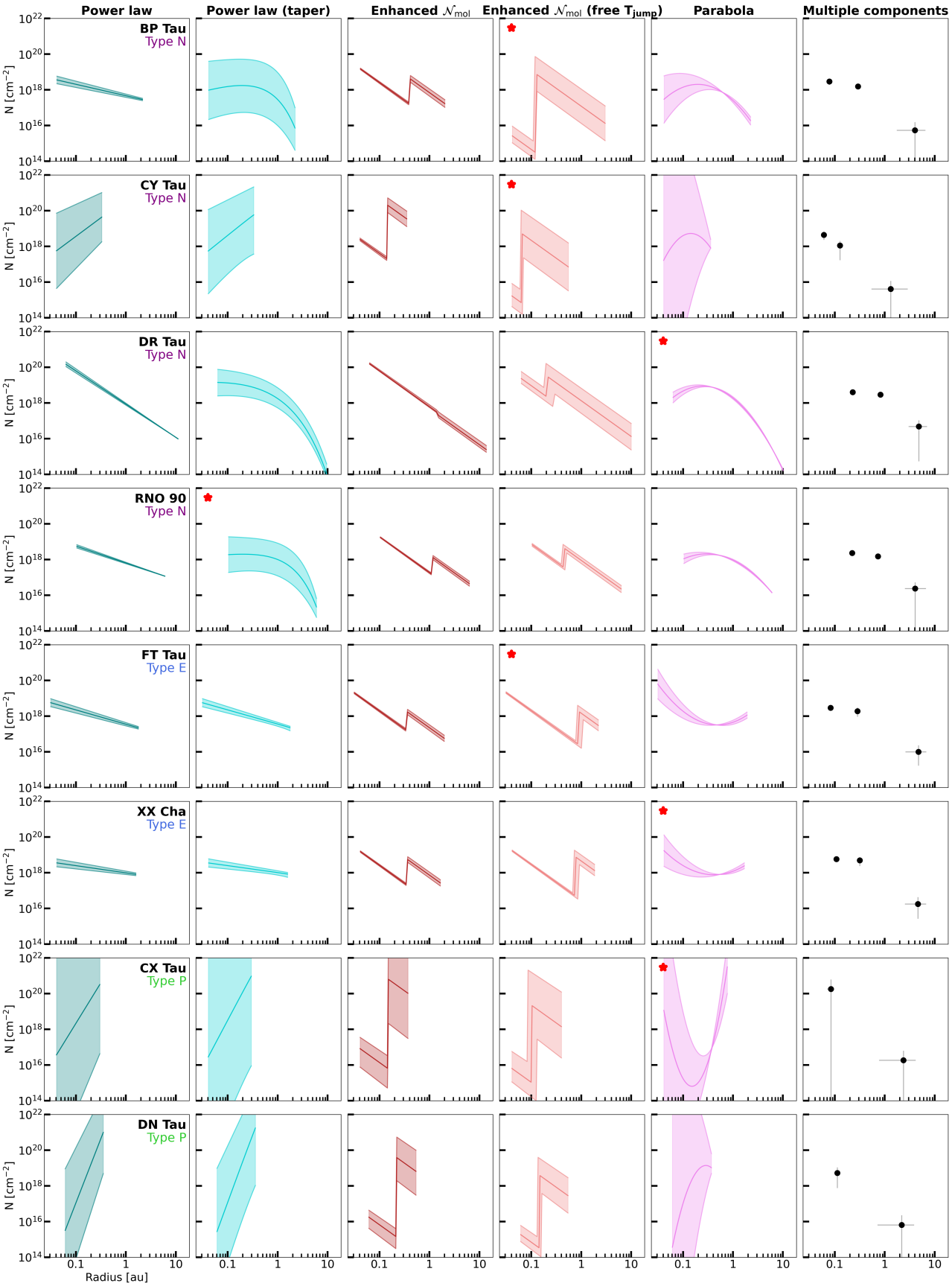

Fig. 3: Profiles and multiple components (rightmost panel) fitted for our sample of compact disks using a line width of 4.71 km s^{-1}. The shaded area is the 1σ-confidence interval, given the uncertainties listed in Tables D.2. The red stars in the top-left corner indicate the best fitting profiles for each disk (see Table D.1). We note that the best-fitting profile for DN Tau is highlighted in Figure D.1.

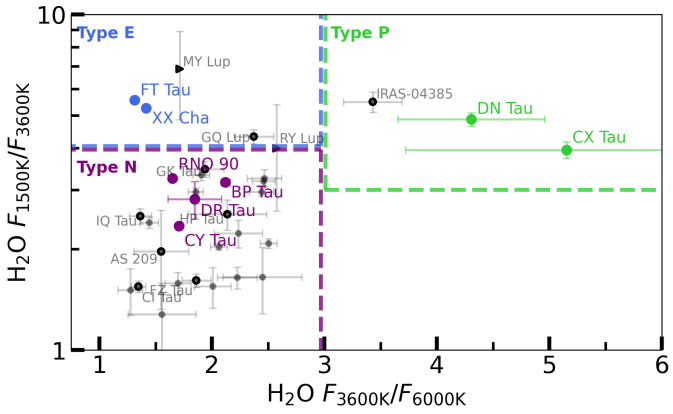

Fig. 4: Ratios of the 3600 K/6000 K and 1500 K/3600 K line fluxes, used to investigate the respective strength of each H_2O reservoir. The grey data points are adapted from Banzatti et al. (2025) (see their Table 3), where we have highlighted those analysed by Romero-Mirza et al. (2024) and potential Type P sources (i.e., MY Lup, RY Lup and IRAS-04385). The coloured data points indicate the line ratios of our sample of compact disks. See Section 5.1 for a discussion on the different types.

systems. Within our sample of compact disks, many of them may behave just like large and structured disks, while only a limited number actually show cold H_2O emission to be strongly enhanced, likely due to radial drift.

5.1. Profile types and H_2O reservoirs

Given the different observed behaviours (see Section 4.1) and the observed line fluxes, we propose to categorise planet-forming disks in at least three different types, based on their H_2O reservoirs: Type N, Type E, and Type P (as already highlighted in Figures 1 and 4). Type N includes the "Normal" disks, which show all three H_2O reservoirs (hot with T >800 K, intermediate with 400< T <800 K, and cold with T <400 K). The cold reservoir is present following the temperature gradient, expected to be present in all disks, but not strongly enhanced suggesting that radial drift is not efficiently replenishing the inner disk with icy pebbles. These disks can be found in the lower-left corner of Figure 4, where both ratios (F_{1500K}/F_{3600K} and F_{3600K}/F_{6000K}) have low values. We expect many of the large and structured disks to be part of this category.

The Type E disks include those with very strong cold H_2O gas reservoirs, which appear to be significantly enhanced, suggesting efficient radial drift. These disks can be found in the top left corner of Figure 4, indicating their large cold H_2O reservoirs by large values for F_{1500K}/F_{3600K}, while their values for F_{3600K}/F_{6000K} are similar to the Type N disks.

Finally, Type P indicates the H_2O-poor (or CO_2-rich; Pontoppidan et al. 2010; Vlasblom et al. 2025) disks, whose spectra are generally devoid of H_2O, but still show strong emission from the cold reservoir. Emission from the other two components is often found to be weak and the emission present can be fitted with either a hot or an intermediate temperature. The lack of H_2O emission from both components (i.e., strong emission from both hot and intermediate) could potentially be due to a small inner cavity depleting the reservoirs in these components (Grant et al. 2023; Vlasblom et al. 2024). The cold component could still be prevalent due to radial drift, especially since snowlines are pushed further out in disks with cavities, holding for both the inner and outer regions (Temmink et al. 2023; Vlasblom et al. 2024). These H_2O-poor disks can be found in the top right corner of Figure 4, with high values for both F_{1500K}/F_{3600K} and F_{3600K}/F_{6000K}. We note that the boundaries for the different types in Figure 4 are arbitrary. To empirically determine the boundaries between the different types, a larger number of disks needs to be consistently analysed. We leave this for future work (Temmink et al. in prep.).

Based on our analysis of the 8 compact disks in the MINDS sample, we suggest that BP Tau, CY Tau, DR Tau, and RNO 90 can all be considered as Type N disks, while FT Tau and XX Cha are the only two compact disks with very strong cold H_2O reservoirs: we consider them to be Type E disks. CX Tau and DN Tau are considered to be Type P disks. Using this categorisation we suggest that the Type N disks can best be described (that is, lowest χ^2_{red}-values) by profiles with jump abundances at higher temperatures or upward parabola, which also resembles the power law profile with a strong exponential taper. The Type E disks are the ones with a jump abundance occurring at low temperatures (T <250 K), have slow monotonically decreasing power laws, and may be described by a shallow downward parabola. On the other hand, the Type P disks likely have rising power law profiles or jump abundances occurring at the intermediate temperatures. Furthermore, their parabolas have a strong minimum.

The distinction between the different groups also becomes

visible when investigating the contribution (with respect to the maximum flux in the observed spectrum) of the 50 individual slab models within the different profiles. As we are fitting 50 different slab models, if they all contributed equally, they would each reach a maximum contribution of 2% at every wavelength. Figure 5 displays the flux contribution of the slab models for DR Tau (top panel, Type N), FT Tau (middle panel, Type E), and CX Tau (bottom panel, Type P). The contributions for DR Tau show that the hot component is the weakest (≤1.5%), as expected from upward parabola, while the intermediate and cold reservoirs are overall of similar strength (~3-4%) given the increasing emitting areas with decreasing temperature. For FT Tau, the hot and intermediate reservoirs are of similar strength (~2%), while the cold reservoir has the strongest contribution (≤6%). The contributions for CX Tau show similar strengths in the hot and cold H_2O reservoirs (≤8%), but a negligible intermediate component, as expected from the downward parabola. While slab models probing the hot and cold reservoirs may have similar maximum contributions, fewer hot H_2O slabs contribute this much to the spectrum and the spectrum is dominated by the cold reservoir overall. Additionally, we want to emphasise that the best-fitting profile dictates the outcome of Figure 5: while the contributions for CX Tau, because of the parabola, have a strong contribution of the hot component, those of DN Tau (both Type P disks) will lack the hot component and have significant contributions from the intermediate component as the spectrum is best-fitted by a jump abundance at a temperature of $T_{\rm jump}$ ~600 K. Finally, we note that the line-to-continuum ratio of CX Tau is much lower (factor of ≥5) than for the other two sources, highlighting that even the higher percental contributions may not be as noticeable as for the other sources.

5.2. Role of substructures

With our sample of compact disks now categorised, we highlight that the analysis of the ALMA visibilities of some of our sources have suggested that these rather compact disks may harbour substructures. In particular, gaps and rings have been proposed for the outer regions (>15 au) of BP Tau (Jennings et al. 2022; Zhang et al. 2023; Gasman et al. 2025), DN Tau (Long et al. 2018; Zhang et al. 2023), DR Tau (Jennings et al. 2022; Zhang et al. 2023; Gasman et al. 2025), and FT Tau (Long et al. 2018; Jennings et al. 2022; Zhang et al. 2023). With substructures hypothesised in disks across all three types, it is clear that the role of substructures in setting the inner disk H_2O reservoirs is not yet well understood (see also Gasman et al. 2025). Furthermore, as modelling works have shown that the influence depends on the gap location, the time at which the structure formed, and how leaky the traps are, this implies that substructures may play a very diverse role in setting the inner disk reservoirs (Kalyaan et al. 2023; Sellek et al. 2025; Easterwood et al. 2024). Age may also play a role (Mah et al. 2023), but we note that the majority of our sample consists of sources from the Taurus star-forming region and it can, therefore, be assumed that these disks all have a similar age. Therefore, our sample may be rather homogeneous and a larger sample, consisting of sources from a variety of different star-forming regions and with different ages, is needed to not only investigate the role of the structure formation time, but also the drift timescale (Mah et al. 2023, 2024).

Our introduced types may, therefore, be comprised of a wide variety of disks. Higher-resolution ALMA observations (spatial resolution of <0.1", but preferably as high as possible) and observations with infrared observatories are needed to confirm and further study these substructures and their potential roles in setting the inner disk abundances, as well as hunt for substructures at smaller scales.

5.3. Profile implications

The following section discusses the differences in more detail. In particular, we further highlight the behaviours of the profiles and what this implies. In Section G, we also discuss how well the different profiles fit for each type.

For the Type N disks, we find that all disks prefer a jump abundance at higher temperatures of generally $T_{\rm jump}$ ≳700 K or a downward parabola (maxima generally at temperatures above 600 K). This behaviour suggests a potential depletion of the hotter component with respect to the stronger intermediate and cold components. This 'depletion' could simply mean that the hot H_2O reservoir is not as abundant as the intermediate and cold ones and, therefore, does not follow a simple power law profile, but it may also have a more physical explanation. As suggested by theoretical models (Sellek et al. 2025; Houge et al. 2025), the inward drift of icy pebbles not only increases the molecular reservoirs when crossing the snowlines, but also increases the continuum optical depth (τ) and, therefore, the continuum τ=1 layer may be moved to higher layers and obscure the underlying H_2O reservoirs.

On the other hand, the optical depth of the H_2O lines themselves may play an important role, which could reach values of τ ~3000 (Temmink et al. 2024a). Therefore, it is possible that only the very top region of the emitting layer can be probed, well above the dust continuum τ=1 layer, while the remainder of the reservoir remains invisible given the high optical depths. As the line optical depth is found to be higher for the hottest component compared to the cooler components (Temmink et al. 2024a), this may play an important role in setting the observable column density for H_2O in the innermost region.

Finally, the destruction of H_2O could also play a role in depleting the inner regions. One of the main destruction routes in these high atmospheric layers of disks is photodissociation. The photodissociation must, however, occur on timescales faster than the gas-phase formation, which is efficient at > 300 K (Bosman & Bergin 2021), to effectively destroy H_2O. Additionally, H_2O can be destroyed in these layers through collisions with C^+, Si^+, and H^+ (Kamp et al. 2013). There is no consensus on which explanation for the flattening of the profiles in the inner regions is correct, as it may be a combination of all three: dust obscuration, optical depth, and destruction. We expect that it is more than likely that different combinations are preferred by different disks and the importance of each explanation will also differ.

The Type E disks, FT Tau and XX Cha, have most notably the jump abundance at low temperature ($T_{\rm jump}$ <250 K) or a shallow downward parabola. As drift can be expected to play to a certain extent a role in all disks, both smooth and structured, where the leakiness of the substructures determines the inward flow of material (Mah et al. 2023, 2024; Gasman et al. 2025), the cold component should be present in most if not all disks. The strength of the cold component in FT Tau and XX Cha, and therefore the jump in abundance at $T_{\rm jump}$ ~250 K and the slowly decreasing power law, can be explained by an extreme or very efficient inward flux of the icy pebbles, enhancing the abundance of this cold component near the H_2O snowline with respect to the other disks.

We note that not all disks in the Type E category may undergo efficient radial drift. Instead, an accretion outburst that significantly heats up the disk and, therefore, enlarges the emitting area of the cold component may also result in disks falling into

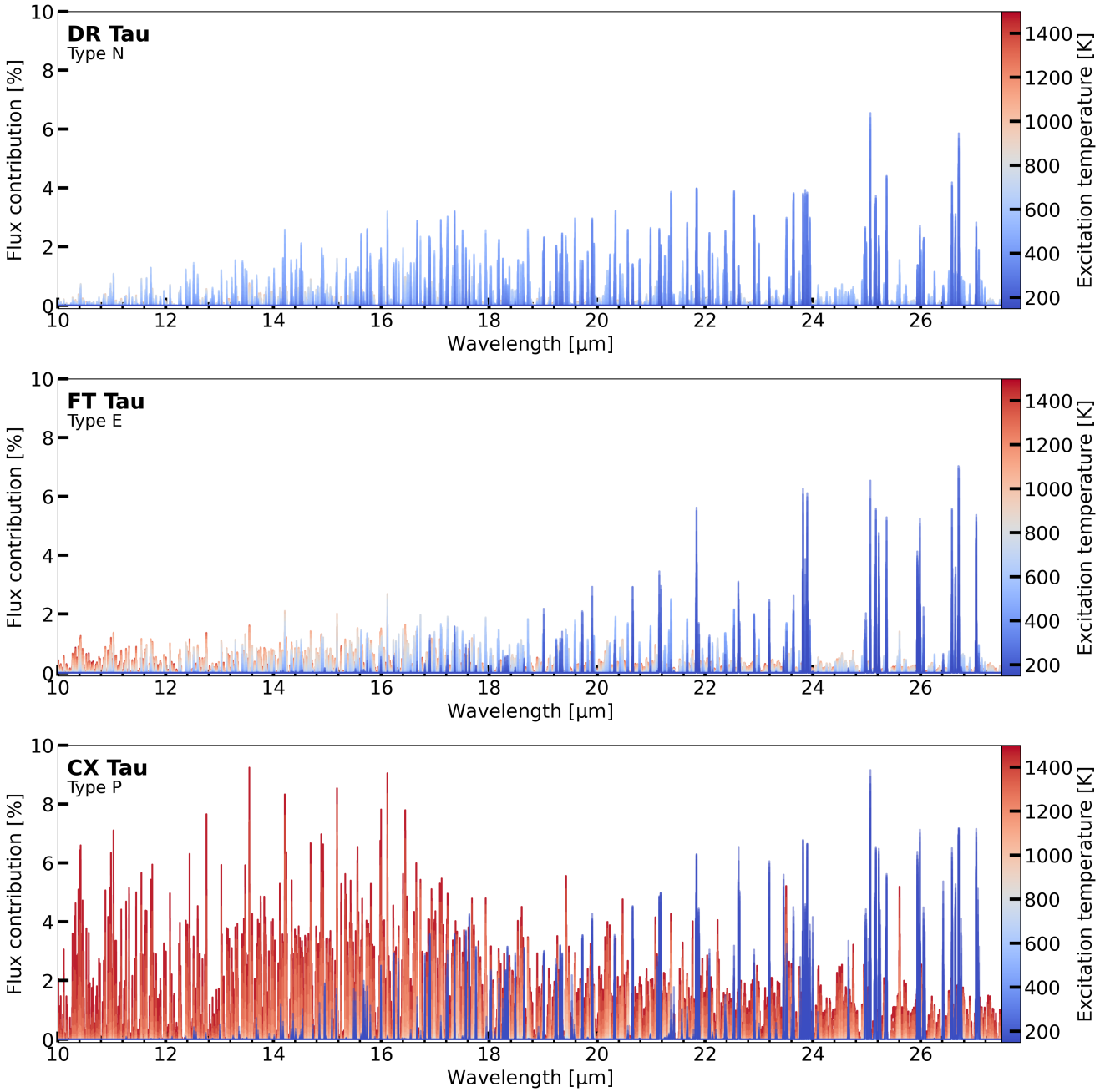

Fig. 5: Contributions of each individual slab model with the colour representing the excitation temperature of the respective slab. The contributions are shown for the best fitting parametric models of DR Tau (Type N), FT Tau (Type E), and CX Tau (Type P). The contributions are taken as the percentage with respect to the maximum line flux in the full model. We note that the maximum line flux of CX Tau is at least a factor of 5 lower than that of the other two types.

this category. In particular, it has been found that XX Cha is highly variable in its accretion (Claes et al. 2022). Even though its variability timescales have not yet been constrained, the observed variation with the X-shooter instrument is on a scale of almost 2 dex (i.e., a factor of 100). Therefore, the strong cold component of XX Cha may be due to its strong variably accretion instead of efficient drift. Furthermore, recent work attributed the strong cold H_2O reservoir observed in the disk of EX Lup to an accretion outburst and the subsequent sublimation of H_2O-ice given the snowline being pushed outwards (Smith et al. 2025). For FT Tau, the other disk identified as a Type E disk in our sample, there are currently no claims of accretion outburst or a strongly variable accretion rate. The reported accretion rate for FT Tau gives values between $\log_{10}\left(\dot{M}_{\rm acc}\right)$ ~-7.5 and -8.9 (Garufi et al. 2014; Gangi et al. 2022) (with $\dot{M}_{\rm acc}$ given in $M_\odot$ year^{-1}), but have not been monitored closely over time. To confirm the role of accretion outbursts and variability in setting the inner disk chemical reservoirs, the accretion rates need to be monitored over an extended period of time to also infer the variability timescales. Also, if present, a larger sample of these sources needs to be observed with JWST-MIRI/MRS and analysed in a consistent manner.

The preferred parametrisations of CX Tau and DN Tau, the Type P disks, include a monotonically increasing power law, a

jump abundance at the intermediate temperatures, and a downward parabola. These profiles all imply a depletion of the hot or intermediate H_2O component with respect to the colder reservoir, which is clearly the strongest. This may suggest a potential dust and gas cavity (see, for example, Salyk et al. 2025), where the cold H_2O is most prominent due to sublimation of H_2O ice near the cavity edge (see also Vlasblom et al. 2024).

Finally, we note that Banzatti et al. (2023a) described two compact disks (GK Tau and HP Tau) having an "excess" in their cold H_2O reservoir with respect to a large and structured disk (CI Tau). Here, we find that similar line flux ratios, as for their two compact disks and for our Type N disks, do not necessarily imply an enhancement of the cold H_2O reservoir, but rather a smooth distribution from hot and/or warm to cold. A true enhancement, as found for our Type E disks, produces an even stronger excess in the cold H_2O lines with respect to their warmer/hotter counterparts. This may also imply that CI Tau is actually depleted in the cold H_2O and, therefore, falls to the lower left corner of Figure 4. Therefore, the Type E compact disks of FT Tau and XX Cha most closely conform with the hypothesis posed by Banzatti et al. (2020) and the overall situation appears to be more complex.

Overall, we find that the jump abundance with the jump temperature ($T_{\rm jump}$) kept free is amongst the favoured fit for all three types. Therefore, we suggest that this profile can be fitted to investigate the H_2O reservoirs in all disks. Furthermore, the location of the jump, as discussed for each type above, may suggest to which type the disk belongs.

5.4. Line width comparison

Not yet addressed are the choices for the different line widths: a fixed value of 4.71 km s^{-1} or the sum in quadrature of a fixed turbulent line width and the thermal line width, given the temperature of the slab model. Intuitively, the quadrature line profiles may be preferred, as the line width changes accordingly with the temperature. One downside is that the strength of turbulence is not known in the inner regions of these disks, therefore the turbulent component of the line width (fixed to 1 km s^{-1}) may be stronger or weaker. Thus far, a few studies have measured the turbulence in the outer regions of large disks using ALMA, resulting in values of < 0.2 km s^{-1} (Paneque-Carreño et al. 2024) or up to ~35% of the sound speed ($<0.35c_s$; Flaherty et al. 2015, 2017, 2020). We find that seven out of eight of our disks prefer the fixed value of 4.71 km s^{-1}. This may suggest that the inner regions of these disks are more turbulent and higher values need to be assumed for the turbulent component ($\Delta V_{\rm turb}$ >1.0 km s^{-1}).

The preferred larger line width may be related to the change in the optical depth of the lines, which decreases with larger line widths ($\tau \sim N/\Delta V$, with ΔV the line width). As the quadrature line widths are overall smaller (see also Romero-Mirza et al. 2024), these models will have larger optical depths. Furthermore, it becomes apparent from the contribution plots (Figures G.1-G.3) that the quadrature line profiles have stronger fluxes in certain lines of the cold component (see, for example, transitions around 25.05 or 26.70 μm). Given the added weights to the lines fitted at the longest wavelengths (>20 μm), we expect the fitting method to find the best profile describing the observed spectrum, regardless of the lower sensitivity of the larger wavelengths observed with JWST-MIRI. Therefore, it is possible that the cold component of the majority of our sample is less optically thick compared to the other disks.

Finally, we notice that our profiles show no qualitative differences between the different line widths (see Figures 3 and D.1), except for the parabola of DN Tau which changes between upward and downward. Therefore, we conclude that the choice of line width does not really matter for the profiles, but note that the optical depth of the reservoirs, as discussed above, does depend on the chosen line width.

5.5. Comparisons with previous analyses

In this section, we compare our analysis with the works of Romero-Mirza et al. (2024) and Gasman et al. (2025), who, respectively, fitted (tapered) power-laws to seven other disks and analysed the H_2O emission in ten structured disks. Additionally, we compare our results with the interpretation of the models by Houge et al. (2025).

Romero-Mirza et al. (2024) only used power law and tapered power law profiles (our profiles I and II) to fit the column density distributions of four compact disks (FZ Tau, GK Tau, GQ Tau, and HP Tau) and three larger disks (AS 209, CI Tau, and IQ Tau). They find that all these disks can be well described by a simple power law, while both CI Tau and FZ Tau prefer the exponentially tapered power law, potentially suggesting a ring-like distribution of the H_2O reservoir. All disks are also captured in the analysis of Banzatti et al. (2025) and are, therefore, displayed in Figure 4, in which we have highlighted their respective positions. All of them, except for maybe GQ Lup, fall within our selection of Type N disks. GQ Lup may also be a Type N disk, given that it is located towards the lower right of Figure 4 with respect to FT Tau and XX Cha and has, therefore, a stronger intermediate component. As stated before, the current definition of the types on Figure 4 is somewhat arbitrary and refining the boundaries for each disk type requires a larger sample of sources, which will be addressed in future work (Temmink et al. in prep.). We also cannot exclude the possibility that other behaviours and types may exist outside the parameter space covered by the 8 disks in our sample. As all disks analysed by Romero-Mirza et al. (2024) may be Type N disks, their profiles can indeed be described by power laws (similar to CY Tau), but may also be represented by jump abundances at higher temperatures or upward parabolas.

Gasman et al. (2025) compared a sample of 10 structured disks and put their H_2O emission in context with respect to DR Tau. They note that the H_2O reservoirs are complicated for these structured disks and that the H_2O reservoirs strongly depend on the age of the system, the mechanisms that open a gap in the outer disk, and the leakiness of such substructures (see also Mah et al. 2024). We note that BP Tau and DR Tau are the two disks overlapping between their sample and ours, highlighting that compact disks may be structured as well. Relative to DR Tau, there is a distinct group of large structured disks (CI Tau, DL Tau, GW Lup, and V1094 Sco) that have a weaker cold H_2O reservoir, which may end up in the lower left corner of Figure 4, where the position of CI Tau is already highlighted. Another group of structured disks (SY Cha and Sz 98) shows, on the other hand, a very strong cold component (stronger than DR Tau) and may, therefore, end up in the upper left corner of Figure 4 near FT Tau and XX Cha. This suggests that the H_2O reservoirs of planet-forming disks are much more complicated and one cannot simply separate them into different types based on their size and/or dust structures, as already discussed in Section 5.3.

Finally, we compare our best-fitting profiles to the predicted model column density profiles by Houge et al. (2025) (for a star with L_*=4 $L_\odot$, see Figure 6). Their column density profiles are given for the observable H_2O reservoir above the τ=1 layer at 20 μm. Their predictions are given for a fixed ratio between

the chemical and mixing timescales (t_{chem}/t_{mix}=0.01) or for a fixed chemical timescale (t_{chem}=10 years) with a radially varying mixing timescale. Furthermore, their models include three types of dust models: fragile (v_{frag}=1 m s^{-1}), composition-dependent (v_{frag}=1-10 m s^{-1}), and resistant (v_{frag}=10 m s^{-1}). They find that for sufficient fragile dust (i.e., in the fragile or composition-dependent cases) the column density is set by the vapour-to-dust mass ratio and the dust opacity, as the profiles for those models do not strongly depend on any disk properties and, therefore, do not evolve over time (see also Sellek et al. 2025). While a direct comparison with the models of Houge et al. (2025) cannot be made given the stellar parameters used in their models, we compare the overall shape of the models with our best-fitting column density profiles in Figure 6. In particular, we make the comparisons with the models with a fixed chemical timescale and radially varying vertical mixing for the different dust types at a time of 1 Myr, an appropriate assumed age for the majority of our sources (see, for example, Krolikowski et al. 2021; Luhman 2023).

Qualitatively, the models and observations agree in the sense that the column density profiles decrease towards larger radii. However, our profiles decrease or flatten off towards the inner regions (see, for example, DR Tau and RNO 90). This could be due to the fact that the expression used by Houge et al. (2025) to derive the abundance of water in the surface layers assumes that the chemical timescale (i.e., the destruction timescale) is always much shorter than the mixing timescale. Under their assumptions, the abundance should saturate inside 0.16 au at a level equal to that of the midplane, resulting in the profile flattening off. This level, namely the limit of $N \sim 10^{20}$ cm^{-2} explored by Sellek et al. (2025), would be equivalent to negligible destruction under the assumption that the H_2O and dust particles behave the same and on similar timescales (that is, as long as the dust is not depleted on faster timescales than the H_2O). Our best-fitting profiles, except for the outer regions of CX Tau, do not exceed a column density of $N \sim 10^{20}$ cm^{-2}, which is in agreement with the limit proposed by Sellek et al. (2025).

Quantitatively, the retrieved column densities fall below all the model profiles for many of our sources, even for the most conservative model predictions with the fragile dust. On the one hand, while their expected column density profiles are based on the increased dust obscuration following radial drift, the importance of the optical depth of the H_2O lines themselves is not explored, which may be important (as discussed in Section 5.3). Alternatively, this may suggest that for our sample of disks the ratio of the chemical and mixing timescales is smaller than their assumptions. This may result from shorter photodissociation timescales which are typically expected to be <1 year in the upper most layers of the disk (Bosman & Bergin 2021, Vlasblom et al. in prep.) and depend source-by-source on the stellar properties (i.e., the UV irradiation field). This may suggest that a chemical timescale of t_{chem}=10 yr may be too long. Future 2D models should further investigate the physical and chemical processing of H_2O in the inner regions and explore how effective the combination of increased dust obscuration following radial drift and line optical depth are.

5.6. Other molecular species

While our analysis focuses solely on the H_2O emission, the spectra of these compact disks contain more molecular species. In this section, we only highlight the other molecular species detected and leave the analysis of this emission for future work. We start by noting that CX Tau (Vlasblom et al. 2025) and DR Tau (Temmink et al. 2024b,a) have dedicated papers analysing their molecular emission and we, therefore, refer the reader to these papers. For the other disks in our sample, the commonly observed species (OH, CO_2, HCN, and C_2H_2) are detected in nearly all disks. For some disks, we also report the (potential) detection of CH_4 in CY Tau and that of some of the isotopologues, such as $^{13}CCH_2$ in CY Tau and both $^{13}CO_2$ and $CO^{18}O$ in DN Tau, which is very similar to CX Tau (Vlasblom et al. 2025). The different species detected in each disk are summarised in Table 3, while Appendix E contains a more elaborate discussion of the detected species.

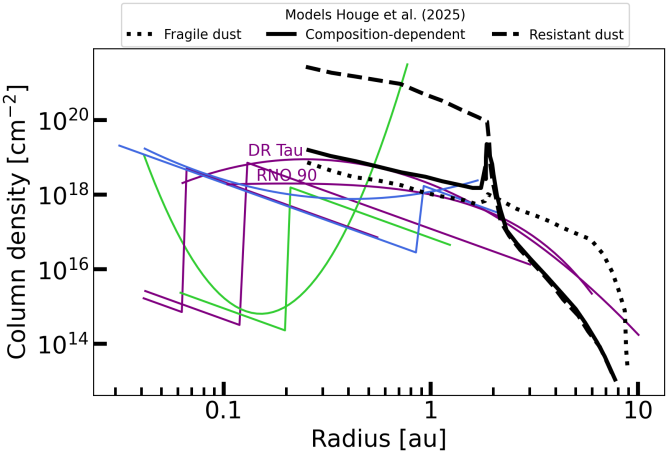

Fig. 6: Comparisons between our parametric models with the lowest χ^2_{red}-values and the prediction from the radially varying vertical models from Houge et al. (2025) for all three tested dust types: fragile (dotted), composition-dependent (solid), and resistant (dashed). The profiles of our disks identified to be Type N are shown in purple, while those of the Type E and Type P disks are displayed in, respectively, blue and green.

6. Conclusions and summary

In this work, we analyse the pure rotational H_2O JWST-MIRI/MRS spectra of 8 millimetre-compact dust disks. We expand upon existing techniques to provide detailed parametric profiles of the column densities beyond (exponentially tapered) power laws. This leads us to infer the best-fitting radial profiles and investigate whether these compact disks show signatures of enhanced reservoirs due to radial drift or whether the overall situation is more complex. Our main conclusions are summarised as follows:

- The pure rotational H_2O spectra of compact dust disks are very different from each other. Half of the disks show similar strengths of the different H_2O reservoirs, conforming with large and structured disks, while others show clear signs of an enhanced cold reservoir, even beyond that found in previous comparisons of compact and large disks.
- Different combinations of parametrisations can be used to describe the observed reservoirs in different disks, leading to the conclusion that planet-forming disks can be grouped into at least three different types (N, E, and P), based on their mid-infrared H_2O spectra.
- The parametrisation that assumes a constant of number of molecules with radius (i.e., the column density is propor-

Table 3: Summary of the other molecules detected in our sample of disks.

Source	Type	OH	CO_2	$^{13}CO_2$	$CO^{18}O$	HCN	C_2H_2	$^{13}CCH_2$	CH_4
BP Tau	N	✓	✓	×	×	✓	×	×	×
CX Tau$^{\alpha}$	P	✓	✓	✓	✓(?)	✓	✓	×	×
CY Tau	N	✓	✓	×	×	✓	✓	✓	✓(?)
DN Tau	P	✓	✓	✓	✓(?)	×	×	×	×
DR Tau$^{\alpha}$	N	✓	✓	×	×	✓	✓	×	×
FT Tau	E	✓	✓	×	×	✓	✓	×	×
RNO 90	N	✓	✓	×	×	✓	✓	×	×
XX Cha	E	✓	✓	×	×	✓	✓	×	×

Notes. $^{\alpha}$: see Vlasblom et al. (2025) for the molecules detected in CX Tau and Temmink et al. (2024b,a) for those in DR Tau.

tional to negative the square of the radius) and has a jump (either an enhancement or depletion) in the abundance at a free temperature is able to provide a good fit for the column density profiles for all disks. The temperature of the jump varies per disk but is found to be similar within each of the different types (N, E, or P).

– We find that the column density profiles, and therefore the distribution of the H_2O reservoirs, are generally best fitted with a fixed line width of ΔV=4.71 km s^{-1}. As the quadrature sum is intuitively and physically more correct, this may suggest that the turbulence is stronger in the inner disk and, therefore, a larger value for the turbulent component needs to be assumed ($\Delta V_{\rm turb}$ >1 km s^{-1}).
– Overall, a good agreement is found between the column densities retrieved through a multiple component analysis and the profiles obtained through the parametric models. The parametric models show that one cannot assume a simple power law through the column densities derived from a multiple component fit, but it is recommended to fit one of the other parametric models used throughout this work.

This work has shown that not all millimetre-compact disks have signatures of strongly enhanced cold H_2O reservoirs following radial drift. Instead, half of our sample behaves similarly to larger, more structured disks. Therefore, we have introduced a new categorisation, given the behaviour of the H_2O reservoirs seen for our disks: Type N, Type E, and Type P disks. Here, N stands for "Normal" disks, whose spectra have contributions from all components (hot, intermediate, and cold). Type P disks are the H_2O-poor disks, whose spectra are dominated by other molecular species, yet have a strong contribution from the cold reservoir. Finally, the Type E disks are the ones that show enhanced cold H_2O, that may be the result of the strong inwards drift of icy pebbles or, perhaps, the product of an accretion outburst that pushes out the H_2O and increases the emitting area of the cold H_2O reservoir. Only two of our 8 compact disks fit into this final category, further highlighting that not all compact disks have enhanced cold H_2O reservoirs. These three types provide a new classification of disks, purely based on their rotational H_2O emission and may be used to further explore trends involving system properties. Higher resolution ALMA observations and/or observations with infrared interferometers are required to further study the occurrence of substructures in these disks, on both small and large scales, and how they may affect the observable reservoirs.

Acknowledgements. The authors would like to thank the referee for many thoughtful, constructive comments that helped improve the manuscript.

This work is based on observations made with the NASA/ESA/CSA James Webb Space Telescope. The data were obtained from the Mikulski Archive for Space Telescopes at the Space Telescope Science Institute, which is operated by the Association of Universities for Research in Astronomy, Inc., under NASA contract NAS 5-03127 for JWST. These observations are associated with program #1282. The following National and International Funding Agencies funded and supported the MIRI development: NASA; ESA; Belgian Science Policy Office (BELSPO); Centre Nationale d'Etudes Spatiales (CNES); Danish National Space Centre; Deutsches Zentrum fur Luft- und Raumfahrt (DLR); Enterprise Ireland; Ministerio De Economía y Competividad; Netherlands Research School for Astronomy (NOVA); Netherlands Organisation for Scientific Research (NWO); Science and Technology Facilities Council; Swiss Space Office; Swedish National Space Agency; and UK Space Agency.

M.T., A.D.S., E.F.v.D., and M.V. all acknowledge support from the ERC grant 101019751 MOLDISK. D.G. thanks the Belgian Federal Science Policy Office (BELSPO) for the provision of financial support in the framework of the PRODEX Programme of the European Space Agency (ESA). E.F.v.D. also acknowledges support the Danish National Research Foundation through the Center of Excellence "InterCat" (DNRF150). E.F.v.D., I.K., and A.M.A. acknowledge support from grant TOP-1 614.001.751 from the Dutch Research Council (NWO). T.H., K.S. and M.S. acknowledge support from the European Research Council under the Horizon 2020 Framework Program via the ERC Advanced Grant Origins 83 24 28. A.C.G. acknowledges support from PRIN-MUR 2022 20228JPA3A "The path to star and planet formation in the JWST era (PATH)" funded by NextGeneration EU and by INAF-GoG 2022 "NIR-dark Accretion Outbursts in Massive Young stellar objects (NAOMY)" and Large Grant INAF 2022 "YSOs Outflows, Disks and Accretion: towards a global framework for the evolution of planet forming systems (YODA)". G.P. gratefully acknowledges support from the Carlsberg Foundation, grant CF23-0481 and from the Max Planck Society. B.T. is a Laureate of the Paris Region fellowship program, which is supported by the Ile-de-France Region and has received funding under the Horizon 2020 innovation framework program and Marie Sklodowska-Curie grant agreement No. 945298.

This work also has made use of the following software packags that have not been mentioned in the main text: NumPy, SciPy, Astropy, Matplotlib, pandas, IPython, Jupyter (Harris et al. 2020; Virtanen et al. 2020; Astropy Collaboration et al. 2013, 2018, 2022; Hunter 2007; pandas development team 2020; Pérez & Granger 2007; Kluyver et al. 2016)

References

Ardila, D. R., Basri, G., Walter, F. M., Valenti, J. A., & Johns-Krull, C. M. 2002, ApJ, 567, 1013
Argyriou, I., Glasse, A., Law, D. R., et al. 2023, A&A, 675, A111
Astropy Collaboration, Price-Whelan, A. M., Lim, P. L., et al. 2022, ApJ, 935, 167
Astropy Collaboration, Price-Whelan, A. M., Sipőcz, B. M., et al. 2018, AJ, 156, 123
Astropy Collaboration, Robitaille, T. P., Tollerud, E. J., et al. 2013, A&A, 558, A33
Banzatti, A., Abernathy, K. M., Brittain, S., et al. 2022, AJ, 163, 174
Banzatti, A., Meyer, M. R., Bruderer, S., et al. 2012, ApJ, 745, 90
Banzatti, A., Pascucci, I., Bosman, A. D., et al. 2020, ApJ, 903, 124
Banzatti, A., Pascucci, I., Edwards, S., et al. 2019, ApJ, 870, 76
Banzatti, A., Pontoppidan, K. M., Carr, J. S., et al. 2023a, ApJ, 957, L22
Banzatti, A., Pontoppidan, K. M., Pére Chávez, J., et al. 2023b, AJ, 165, 72
Banzatti, A., Pontoppidan, K. M., Salyk, C., et al. 2017, ApJ, 834, 152
Banzatti, A., Salyk, C., Pontoppidan, K. M., et al. 2025, AJ, 169, 165
Barvainis, R. 1987, ApJ, 320, 537
Blevins, S. M., Pontoppidan, K. M., Banzatti, A., et al. 2016, ApJ, 818, 22
Bosman, A. D. & Bergin, E. A. 2021, ApJ, 918, L10
Bosman, A. D., Bergin, E. A., Calahan, J., & Duval, S. E. 2022, ApJ, 930, L26

Bushouse, H., Eisenhamer, J., Dencheva, N., et al. 2024, JWST Calibration Pipeline
Carnall, A. C. 2017, arXiv e-prints, arXiv:1705.05165
Claes, R. A. B., Manara, C. F., Garcia-Lopez, R., et al. 2022, A&A, 664, L7
Collings, M. P., Anderson, M. A., Chen, R., et al. 2004, MNRAS, 354, 1133
Colmenares, M. J., Bergin, E. A., Salyk, C., et al. 2024, ApJ, 977, 173
Dawson, R. I. & Johnson, J. A. 2018, ARA&A, 56, 175
Dullemond, C. P. & Dominik, C. 2004, A&A, 417, 159
Dullemond, C. P., Dominik, C., & Natta, A. 2001, ApJ, 560, 957
Easterwood, W., Kalyaan, A., & Banzatti, A. 2024, ApJ, 977, 21
Erb, D. 2022, pybaselines: A Python library of algorithms for the baseline correction of experimental data, Zenodo
Facchini, S., Birnstiel, T., Bruderer, S., & van Dishoeck, E. F. 2017, A&A, 605, A16
Facchini, S., van Dishoeck, E. F., Manara, C. F., et al. 2019, A&A, 626, L2
Fang, M., Pascucci, I., Edwards, S., et al. 2018, ApJ, 868, 28
Flaherty, K., Hughes, A. M., Simon, J. B., et al. 2020, ApJ, 895, 109
Flaherty, K. M., Hughes, A. M., Rose, S. C., et al. 2017, ApJ, 843, 150
Flaherty, K. M., Hughes, A. M., Rosenfeld, K. A., et al. 2015, ApJ, 813, 99
Foreman-Mackey, D., Hogg, D. W., Lang, D., & Goodman, J. 2013, PASP, 125, 306
Gaia Collaboration, Brown, A. G. A., Vallenari, A., et al. 2018, A&A, 616, A1
Gangi, M., Antoniucci, S., Biazzo, K., et al. 2022, A&A, 667, A124
Garufi, A., Podio, L., Kamp, I., et al. 2014, A&A, 567, A141
Gasman, D., Temmink, M., van Dishoeck, E. F., et al. 2025, A&A, 694, A147
Gasman, D., van Dishoeck, E. F., Grant, S. L., et al. 2023, A&A, 679, A117
Grant, S. L., van Dishoeck, E. F., Tabone, B., et al. 2023, ApJ, 947, L6
Greenwood, A. J., Kamp, I., Waters, L. B. F. M., Woitke, P., & Thi, W. F. 2019, A&A, 626, A6
Harris, C. R., Millman, K. J., van der Walt, S. J., et al. 2020, Nature, 585, 357
Henning, T., Kamp, I., Samland, M., et al. 2024, PASP, 136, 054302
Herczeg, G. J. & Hillenbrand, L. A. 2014, ApJ, 786, 97
Houge, A., Krijt, S., Banzatti, A., et al. 2025, MNRAS, 537, 691
Hunter, J. D. 2007, Computing in Science & Engineering, 9, 90
Jennings, J., Tazzari, M., Clarke, C. J., Booth, R. A., & Rosotti, G. P. 2022, MNRAS, 514, 6053
Kaeufer, T., Min, M., Woitke, P., Kamp, I., & Arabhavi, A. M. 2024, A&A, 687, A209
Kalyaan, A., Pinilla, P., Krijt, S., et al. 2023, ApJ, 954, 66
Kamp, I., Henning, T., Arabhavi, A. M., et al. 2023, Faraday Discussions, 245, 112
Kamp, I., Thi, W. F., Meeus, G., et al. 2013, A&A, 559, A24
Kluyver, T., Ragan-Kelley, B., Pérez, F., et al. 2016, in Positioning and Power in Academic Publishing: Players, Agents and Agendas, ed. F. Loizides & B. Schmidt, IOS Press, 87 – 90
Krolikowski, D. M., Kraus, A. L., & Rizzuto, A. C. 2021, AJ, 162, 110
Lienert, J. L., Bitsch, B., & Henning, T. 2024, A&A, 691, A72
Long, F., Herczeg, G. J., Harsono, D., et al. 2019, ApJ, 882, 49
Long, F., Pinilla, P., Herczeg, G. J., et al. 2018, ApJ, 869, 17
Luhman, K. L. 2023, AJ, 165, 37
Mah, J., Bitsch, B., Pascucci, I., & Henning, T. 2023, A&A, 677, L7
Mah, J., Savvidou, S., & Bitsch, B. 2024, A&A, 686, L17
Manara, C. F., Fedele, D., Herczeg, G. J., & Teixeira, P. S. 2016, A&A, 585, A136
Morbidelli, A., Lunine, J. I., O'Brien, D. P., Raymond, S. N., & Walsh, K. J. 2012, Annual Review of Earth and Planetary Sciences, 40, 251
Najita, J. R., Carr, J. S., Strom, S. E., et al. 2010, ApJ, 712, 274
Newville, M., Otten, R., Nelson, A., et al. 2024, lmfit/lmfit-py: 1.3.2
Nguyen, D. C., Brandeker, A., van Kerkwijk, M. H., & Jayawardhana, R. 2012, ApJ, 745, 119
pandas development team, T. 2020, pandas-dev/pandas: Pandas
Paneque-Carreño, T., Izquierdo, A. F., Teague, R., et al. 2024, A&A, 684, A174
Pascucci, I., Apai, D., Hardegree-Ullman, E. E., et al. 2008, ApJ, 673, 477
Pérez, F. & Granger, B. E. 2007, Computing in Science and Engineering, 9, 21
Perotti, G., Christiaens, V., Henning, T., et al. 2023, Nature, 620, 516
Pinilla, P., Benisty, M., Waters, R., Bae, J., & Facchini, S. 2024, A&A, 686, A135
Pontoppidan, K. M., Salyk, C., Banzatti, A., et al. 2024, ApJ, 963, 158
Pontoppidan, K. M., Salyk, C., Blake, G. A., et al. 2010, ApJ, 720, 887
Rieke, G. H., Wright, G. S., Böker, T., et al. 2015, PASP, 127, 584
Rigby, J., Perrin, M., McElwain, M., et al. 2023, PASP, 135, 048001
Roccatagliata, V., Franciosini, E., Sacco, G. G., Randich, S., & Sicilia-Aguilar, A. 2020, A&A, 638, A85
Romero-Mirza, C. E., Banzatti, A., Öberg, K. I., et al. 2024, ApJ, 975, 78
Salyk, C., Pontoppidan, K. M., Banzatti, A., et al. 2025, AJ, 169, 184
Salyk, C., Pontoppidan, K. M., Blake, G. A., Najita, J. R., & Carr, J. S. 2011, ApJ, 731, 130
Schwarz, K. R., Henning, T., Christiaens, V., et al. 2024, ApJ, 962, 8
Sellek, A. D., Vlasblom, M., & van Dishoeck, E. F. 2025, A&A, 694, A79
Simon, M., Guilloteau, S., Di Folco, E., et al. 2017, ApJ, 844, 158
Smith, S. A., Romero-Mirza, C. E., Banzatti, A., et al. 2025, ApJ, 984, L51
Tabone, B., Bettoni, G., van Dishoeck, E. F., et al. 2023, Nature Astronomy, 7, 805
Temmink, M., Booth, A. S., van der Marel, N., & van Dishoeck, E. F. 2023, A&A, 675, A131
Temmink, M., van Dishoeck, E. F., Gasman, D., et al. 2024a, A&A, 689, A330
Temmink, M., van Dishoeck, E. F., Grant, S. L., et al. 2024b, A&A, 686, A117
Trapman, L., Facchini, S., Hogerheijde, M. R., van Dishoeck, E. F., & Bruderer, S. 2019, A&A, 629, A79
Virtanen, P., Gommers, R., Oliphant, T. E., et al. 2020, Nature Methods, 17, 261
Vlasblom, M., Temmink, M., Grant, S. L., et al. 2025, A&A, 693, A278
Vlasblom, M., van Dishoeck, E. F., Tabone, B., & Bruderer, S. 2024, A&A, 682, A91
Wells, M., Pel, J. W., Glasse, A., et al. 2015, PASP, 127, 646
Woitke, P., Kamp, I., Antonellini, S., et al. 2019, PASP, 131, 064301
Woitke, P., Thi, W. F., Arabhavi, A. M., et al. 2024, A&A, 683, A219
Wright, G. S., Rieke, G. H., Glasse, A., et al. 2023, PASP, 135, 048003
Wright, G. S., Wright, D., Goodson, G. B., et al. 2015, PASP, 127, 595
Zhang, S., Kalscheur, M., Long, F., et al. 2023, ApJ, 952, 108

[1] Leiden Observatory, Leiden University, PO Box 9513, 2300 RA Leiden, the Netherlands
e-mail: temmink@strw.leidenuniv.nl
[2] Institute of Astronomy, KU Leuven, Celestijnenlaan 200D, 3001 Leuven, Belgium
[3] Max-Planck-Institut für Extraterrestrische Physik, Giessenbachstraße 1, D-85748 Garching, Germany
[4] Dept. of Astrophysics, University of Vienna, Türkenschanzstr. 17, A-1180 Vienna, Austria
[5] ETH Zürich, Institute for Particle Physics and Astrophysics, Wolfgang-Pauli-Str. 27, 8093 Zürich, Switzerland
[6] Max-Planck-Institut für Astronomie (MPIA), Königstuhl 17, 69117 Heidelberg, Germany
[7] Université Paris-Saclay, Université Paris Cité, CEA, CNRS, AIM, F-91191 Gif-sur-Yvette, France
[8] INAF – Osservatorio Astronomico di Capodimonte, Salita Moiariello 16, 80131 Napoli, Italy
[9] Dublin Institute for Advanced Studies, 31 Fitzwilliam Place, D02 XF86 Dublin, Ireland
[10] Kapteyn Astronomical Institute, Rijksuniversiteit Groningen, Postbus 800, 9700AV Groningen, The Netherlands
[11] Department of Astronomy, Stockholm University, AlbaNova University Center, 10691 Stockholm, Sweden
[12] Earth and Planets Laboratory, Carnegie Institution for Science, 5241 Broad Branch Road, NW, Washington, DC 20015, USA
[13] Department of Physics and Astronomy, University of Exeter, Exeter EX4 4QL, UK
[14] Niels Bohr Institute, University of Copenhagen, NBB BA2, Jagtvej 155A, 2200 Copenhagen, Denmark
[15] Université Paris-Saclay, CNRS, Institut d'Astrophysique Spatiale, 91405, Orsay, France

Appendix A: Velocity shifted slab models

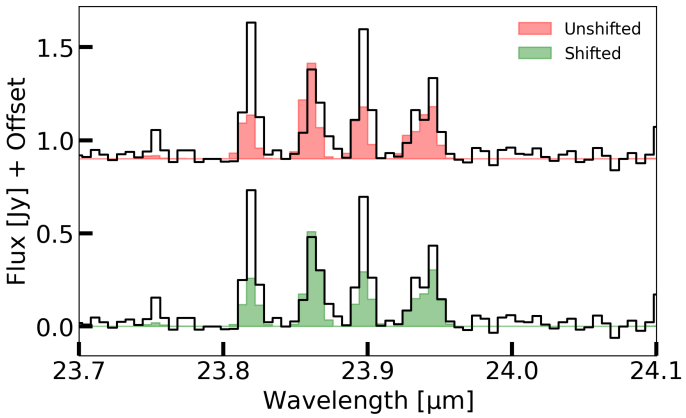

Fig. A.1: Comparison, using DR Tau as a test case, between an unshifted slab model (red) and one shifted by the heliocentric velocity.

Appendix B: Signal-to-noise ratios on the continuum and uncertainties for the observations

Table B.1: S/N-ratios for each subband obtained from the *Exposure Time Calculator*.

Source	ETC S/N-ratio in each subband											
	1A	1B	1C	2A	2B	2C	3A	3B	3C	4A	4B	4C
BP Tau	383.46	428.72	519.87	570.45	900.21	996.66	799.42	827.84	992.3	519.48	301.15	73.06
CX Tau	368.49	422.36	529.29	575.06	794.03	892.06	783.2	835.26	984.43	518.9	339.39	103.01
CY Tau	497.79	557.57	647.37	619.63	736.81	782.54	685.5	666.27	671.04	288.82	155.6	41.29
DN Tau	511.39	584.19	700.23	723.75	921.2	1046.72	961.64	1014.51	1143.0	622.85	427.47	137.28
DR Tau	558.15	624.65	755.79	767.27	994.22	1098.16	968.84	1006.86	1133.53	493.85	265.88	60.77
FT Tau	373.63	414.88	504.52	553.14	769.13	857.08	724.21	754.76	843.66	405.9	245.9	66.0
RNO 90	668.11	719.03	835.31	833.83	1075.98	1194.92	910.9	922.45	1057.8	435.4	219.53	45.73
XX Cha	383.02	423.56	506.03	538.19	740.69	822.55	720.9	753.22	862.37	457.42	283.29	78.24

Appendix C: Slab model fit regions

Table C.1: Fit regions used for the fitting of H_2O transitions.

Molecule	Sources	Fit regions[α]
H_2O	BP Tau, CY Tau, DR Tau, FT Tau, RNO 90, XX Cha	11.717-11.735, 12.56-12.57, 13.128-13.138, 13.2875-13.318, 13.495-13.513, 14.202-14.218, 14.34-14.355, 14.42-14.438, 14.505-14.523, 14.68-14.695, 14.857-14.872, 14.888-14.905, 15.17-15.19, 15.41-15.425, 15.447-15.463, 15.567-15.583, 15.615-15.635, 15.717-15.732, 15.75-15.767, 15.958-15.975, 16.10-16.125, 16.263-16.28, 16.313-16.332, 16.535-16.553, 16.715-16.735, 16.975-16.993, 17.093-17.111, 17.135-17.15, 17.318-17.333, 17.348-17.366, 17.367-17.38, 17.397-17.415, 17.493-17.515, 17.558-17.575, 17.910-17.955, 18.240-18.270, 18.702-18.732, 19.230-19.266, 19.338-19.368, 19.572-19.608, 19.674-19.704, 19.925-19.95, 20.556-20.586 (5), 20.646-20.676 (15), 20.972-21.008 (5), 21.313-21.35 (5), 21.356-21.386 (5), 21.65-21.686 (5), 22.064-22.10 (5), 22.118-22.154 (5), 22.358-22.388 (5), 22.52-22.556 (5), 22.898-22.928 (5), 22.982-23.018 (5), 23.798-23.834 (15), 23.84-23.876 (5), 23.882-23.912 (15), 25.042-25.084 (10), 25.131-25.157 (5), 25.342-25.39 (5), 26.038-26.068 (5), 26.242-26.272 (5), 26.626-26.656 (5), 26.69-26.72 (10), 27.01-27.046 (15)
	CX Tau, DN Tau	11.717-11.735, 12.56-12.57, 13.128-13.138, 13.2875-13.318, 13.495-13.513, 15.958-15.975, 16.10-16.125, 16.263-16.28, 16.313-16.332, 16.535-16.553, 16.715-16.735, 16.975-16.993, 17.093-17.111, 17.135-17.15, 17.318-17.333, 17.348-17.366, 17.367-17.38, 17.397-17.415, 17.493-17.515, 17.558-17.575, 17.910-17.955, 18.240-18.270, 18.702-18.732, 19.230-19.266, 19.338-19.368, 19.572-19.608, 19.674-19.704, 19.925-19.95, 20.556-20.586 (5), 20.646-20.676 (15), 20.972-21.008 (5), 21.313-21.35 (5), 21.356-21.386 (5), 21.65-21.686 (5), 22.064-22.10 (5), 22.118-22.154 (5), 22.358-22.388 (5), 22.52-22.556 (5), 22.898-22.928 (5), 22.982-23.018 (5), 23.798-23.834 (15), 23.84-23.876 (5), 23.882-23.912 (15), 25.042-25.084 (10), 25.131-25.157 (5), 25.342-25.39 (5), 26.038-26.068 (5), 26.242-26.272 (5), 26.626-26.656 (5), 26.69-26.72 (10), 27.01-27.046 (15)

Notes. [α]: values listed in parenthesis in the fit regions denote the chosen weight, w, in Equation 7. If no value is listed, the weight is set to unity.

Appendix D: Fit results

Table D.1: Summary of the results: $\chi^2_{\rm red}$ values.

Source	I		II		III		IV		V		MC	
	4.71	Quad.	4.71	Quad.	4.71	Quad.	4.71	Quad.	4.71	Quad.	4.71	Quad.
BP Tau	157.58	173.89	140.25	145.55	187.20	198.48	**128.52**	143.63	139.37	142.61	117.23	133.22
CX Tau	32.37	29.59	33.01	29.81	29.27	27.95	27.45	27.35	**24.08**	24.74	25.04	21.51
CY Tau	70.80	69.94	72.58	67.00	67.15	78.36	**55.48**	62.22	70.79	64.82	55.39	60.22
DN Tau	45.48	42.03	46.70	43.11	40.43	39.38	33.39	**32.98**	43.14	43.26	27.13	27.88
DR Tau	277.59	327.08	240.21	314.62	279.71	293.29	251.75	293.77	**232.89**	298.08	222.74	243.85
FT Tau	125.18	138.15	125.68	138.39	127.23	144.95	**102.26**	116.22	104.21	123.19	88.35	97.56
RNO 90	286.99	331.84	**265.07**	296.33	341.82	359.50	265.30	291.75	265.45	284.71	254.25	272.68
XX Cha	200.57	197.65	200.45	198.50	211.05	218.82	191.71	191.13	**189.78**	193.44	149.05	161.40

Notes. The Roman numbers have the following meanings: I - Power law fit, II - Power law with exponential taper, III - Jump abundance ($T_{\rm jump}$=400 K), IV - Jump abundance (free $T_{\rm jump}$), V - Parabola in log-space. MC stands for the multiple component analysis.
The bold-faced entries highlight the fitted profile with the lowest value for $\chi^2_{\rm red}$.

Table D.2: Fit values for the profiles with a line width of 4.71 km s^{-1}.

	Power law			Power law with exponential taper				
Source	q	$\log_{10}(N_0)$	p	q	$\log_{10}(N_0)$	p	$\log_{10}(R_{\rm c})$	ϕ
BP Tau	0.57±0.01	17.67±0.09	$0.64^{+0.08}_{-0.09}$	0.57±0.01	$19.27^{+0.81}_{-0.68}$	$-0.86^{+0.52}_{-0.56}$	$-0.70^{+0.39}_{-0.45}$	$0.89^{+0.43}_{-0.21}$
CX Tau	$1.13^{+0.10}_{-0.11}$	$22.87^{+2.55}_{-2.74}$	$-4.54^{+2.26}_{-2.18}$	1.14±0.10	$23.79^{+2.49}_{-3.10}$	$-5.28^{+2.57}_{-2.13}$	$-0.09^{+0.74}_{-0.69}$	$2.51^{+1.66}_{-1.37}$
CY Tau	1.08±0.04	20.64±0.99	$-2.08^{+0.81}_{-0.80}$	1.08±0.04	$20.87^{+1.13}_{-1.07}$	$-2.25^{+0.86}_{-0.91}$	$-0.01^{+0.69}_{-0.67}$	$2.52^{+1.65}_{-1.41}$
DN Tau	1.29±0.08	$24.25^{+1.47}_{-1.62}$	$-7.20^{+1.63}_{-1.52}$	1.28±0.08	$24.73^{+1.45}_{-1.71}$	$-7.65^{+1.72}_{-1.47}$	$-0.16^{+0.78}_{-0.57}$	$2.54^{+1.60}_{-1.36}$
DR Tau	0.44±0.01	17.94±0.06	1.86±0.06	0.45±0.01	$19.97^{+0.26}_{-0.36}$	$-0.39^{+0.30}_{-0.27}$	$-1.04^{+0.24}_{-0.13}$	$0.57^{+0.06}_{-0.03}$
FT Tau	0.56±0.01	17.55±0.09	0.80±0.09	0.56±0.01	17.56±0.09	0.79±0.09	$0.76^{+0.17}_{-0.22}$	$3.52^{+1.03}_{-1.38}$
RNO 90	0.56±0.01	17.81±0.04	$0.94^{+0.06}_{-0.05}$	0.56±0.01	$18.67^{+0.56}_{-0.36}$	$-0.32^{+0.38}_{-0.46}$	$-0.20^{+0.30}_{-0.46}$	$0.94^{+0.38}_{-0.25}$
XX Cha	0.62±0.01	$17.99^{+0.10}_{-0.09}$	0.40±0.09	0.62±0.01	$18.01^{+0.09}_{-0.10}$	$0.39^{+0.09}_{-0.10}$	$0.74^{+0.18}_{-0.23}$	$3.39^{+1.12}_{-1.51}$

	Jump abundance ($T_{\rm jump}$=400 K)			Jump abundance ($T_{\rm jump}$ free)				
Source	q	$\log_{10}(\mathcal{N}_{\rm mol})$	$\log_{10}(F_{\rm scale})$	q	$T_{\rm jump}$	$\log_{10}(\mathcal{N}_{\rm mol})$	$\log_{10}(F_{\rm scale})$	
BP Tau	0.58±0.01	42.42±0.03	$1.44^{+0.12}_{-0.11}$	0.53±0.01	843±28	$38.71^{+0.54}_{-0.38}$	$4.42^{+0.38}_{-0.54}$	-
CX Tau	1.02±0.07	$39.70^{+0.60}_{-1.00}$	$5.02^{+1.25}_{-1.36}$	$0.99^{+0.08}_{-0.07}$	599^{+109}_{-127}	$38.60^{+0.91}_{-0.72}$	$4.32^{+0.83}_{-0.84}$	-
CY Tau	1.05±0.03	41.33±0.06	$3.02^{+0.31}_{-0.30}$	$0.87^{+0.03}_{-0.02}$	989^{+41}_{-42}	$38.25^{+0.69}_{-0.58}$	$3.88^{+0.58}_{-0.68}$	-
DN Tau	1.04±0.05	$39.53^{+0.37}_{-0.60}$	$4.45^{+0.71}_{-0.61}$	$1.03^{+0.06}_{-0.05}$	593^{+52}_{-53}	$38.55^{+0.49}_{-0.37}$	$4.08^{+0.40}_{-0.49}$	-
DR Tau	0.42±0.01	$43.98^{+0.05}_{-0.02}$	-0.13±0.08	0.45±0.01	854^{+62}_{-98}	$43.13^{+0.39}_{-0.26}$	$1.16^{+0.27}_{-0.38}$	-
FT Tau	0.54±0.01	42.27±0.04	1.06±0.08	0.53±0.01	247±18	42.30±0.04	$1.84^{+0.21}_{-0.18}$	-
RNO 90	0.55±0.01	43.25±0.02	0.98±0.06	0.55±0.01	655^{+29}_{-28}	$42.83^{+0.07}_{-0.08}$	1.09±0.08	-
XX Cha	0.61±0.01	42.33±0.04	1.45±0.09	0.59±0.01	258^{+17}_{-16}	42.39±0.03	$2.19^{+0.26}_{-0.20}$	-

	Parabola							
Source	q	$\log_{10}(N_0)$	α	β				
BP Tau	0.57±0.01	$17.40^{+0.11}_{-0.12}$	$-2.56^{+0.43}_{-0.49}$	$0.79^{+0.19}_{-0.17}$	-	-	-	-
CX Tau	$0.77^{+0.05}_{-0.04}$	$23.80^{+1.72}_{-1.97}$	$21.93^{+2.89}_{-4.05}$	$-5.80^{+0.94}_{-0.72}$	-	-	-	-
CY Tau	$1.04^{+0.05}_{-0.04}$	$15.07^{+3.48}_{-2.21}$	$-8.65^{+6.81}_{-4.55}$	$2.22^{+1.00}_{-1.43}$	-	-	-	-
DN Tau	1.25±0.08	$16.15^{+3.89}_{-2.61}$	$-11.01^{+8.33}_{-5.91}$	$4.41^{+1.42}_{-1.97}$	-	-	-	-
DR Tau	0.45±0.01	18.28±0.06	-2.21±0.08	0.79±0.08	-	-	-	-
FT Tau	0.55±0.01	17.65±0.11	$0.97^{+0.28}_{-0.27}$	-0.69±0.10	-	-	-	-
RNO 90	0.56±0.01	$17.97^{+0.04}_{-0.05}$	$-1.34^{+0.10}_{-0.11}$	$0.56^{+0.10}_{-0.09}$	-	-	-	-
XX Cha	0.61±0.01	$18.08^{+0.11}_{-0.10}$	$1.03^{+0.33}_{-0.31}$	0.59±0.12	-	-	-	-

Table D.3: Fit values for the profiles with the quadrature line widths.

	Power law			Power law with exponential taper				
Source	q	$\log_{10}(N_0)$	p	q	$\log_{10}(N_0)$	p	$\log_{10}(R_c)$	ϕ
BP Tau	0.44±0.01	17.02±0.06	$1.39^{+0.05}_{-0.06}$	0.44±0.01	$19.10^{+0.38}_{-0.49}$	$-0.60^{+0.35}_{-0.29}$	$-1.08^{+0.35}_{-0.22}$	$0.57^{+0.09}_{-0.04}$
CX Tau	$0.75^{+0.08}_{-0.06}$	$18.26^{+2.03}_{-0.87}$	$-0.85^{+0.80}_{-1.81}$	$0.77^{+0.08}_{-0.06}$	$18.80^{+2.87}_{-1.18}$	$-1.31^{+1.06}_{-2.61}$	$0.26^{+0.50}_{-0.62}$	$2.42^{+1.71}_{-1.42}$
CY Tau	0.65±0.02	$16.89^{+0.23}_{-0.22}$	$0.91^{+0.19}_{-0.20}$	0.66±0.02	$18.39^{+1.36}_{-1.14}$	$-0.37^{+0.94}_{-1.04}$	$-0.63^{+0.53}_{-0.49}$	$1.12^{+0.93}_{-0.33}$
DN Tau	0.85±0.05	$19.10^{+1.15}_{-0.91}$	$-2.46^{+0.98}_{-1.28}$	0.86±0.05	$19.67^{+1.81}_{-1.15}$	$-3.06^{+1.25}_{-1.97}$	$0.11^{+0.61}_{-0.69}$	$2.09^{+1.87}_{-1.11}$
DR Tau	0.35±0.01	$17.99^{+0.05}_{-0.04}$	2.32±0.04	0.37±0.01	$18.67^{+0.21}_{-0.19}$	1.40±0.26	$0.02^{+0.31}_{-0.26}$	$0.53^{+0.05}_{-0.02}$
FT Tau	0.44±0.01	17.11±0.07	1.37±0.07	0.45±0.01	$17.12^{+0.08}_{-0.07}$	1.36±0.08	$0.90^{+0.07}_{-0.10}$	$3.84^{+0.82}_{-1.24}$
RNO 90	0.41±0.01	$17.50^{+0.03}_{-0.04}$	1.61±0.04	0.43±0.01	$18.58^{+0.21}_{-0.22}$	0.09±0.23	$-0.57^{+0.24}_{-0.16}$	$0.53^{+0.05}_{-0.02}$
XX Cha	0.49±0.01	17.46±0.07	$1.07^{+0.08}_{-0.07}$	0.49±0.01	$17.48^{+0.08}_{-0.07}$	1.05±0.08	$0.90^{+0.07}_{-0.11}$	$3.72^{+0.91}_{-1.53}$

	Jump abundance (T_{jump}=400 K)			Jump abundance (T_{jump} free)				
Source	q	$\log_{10}(\mathcal{N}_{mol})$	$\log_{10}(F_{scale})$	q	T_{jump}	$\log_{10}(\mathcal{N}_{mol})$	$\log_{10}(F_{scale})$	
BP Tau	0.44±0.01	42.78±0.04	0.60±0.08	0.44±0.01	694^{+39}_{-36}	$42.01^{+0.15}_{-0.20}$	$1.28^{+0.20}_{-0.16}$	-
CX Tau	0.75±0.05	$40.58^{+0.34}_{-0.72}$	$3.26^{+1.73}_{-1.11}$	0.72±0.05	549^{+165}_{-255}	$39.36^{+1.48}_{-1.04}$	$3.89^{+0.89}_{-1.07}$	-
CY Tau	0.64±0.02	41.72±0.05	$0.83^{+0.22}_{-0.19}$	0.61±0.02	1044^{+53}_{-61}	$38.55^{+0.93}_{-0.63}$	$3.60^{+0.63}_{-0.91}$	-
DN Tau	0.78±0.03	$40.16^{+0.33}_{-0.57}$	$3.57^{+0.89}_{-0.65}$	0.75±0.03	602^{+57}_{-56}	$38.80^{+0.39}_{-0.27}$	$3.88^{+0.33}_{-0.40}$	-
DR Tau	0.35±0.01	$44.29^{+0.04}_{-0.03}$	-0.57±0.06	0.35±0.01	393^{+19}_{-18}	44.29±0.04	-0.57±0.07	-
FT Tau	0.44±0.01	42.66±0.05	0.55±0.07	0.43±0.01	205^{+20}_{-17}	42.66±0.06	$1.67^{+0.32}_{-0.28}$	-
RNO 90	0.41±0.01	$43.54^{+0.01}_{-0.05}$	$0.23^{+0.06}_{-0.05}$	0.42±0.01	779^{+42}_{-40}	$42.83^{+0.13}_{-0.17}$	$1.00^{+0.16}_{-0.14}$	-
XX Cha	0.48±0.01	42.77±0.04	0.83±0.08	0.47±0.01	214^{+16}_{-14}	$42.79^{+0.05}_{-0.04}$	$1.73^{+0.24}_{-0.21}$	-

	Parabola							
Source	q	$\log_{10}(N_0)$	α	β				
BP Tau	0.44±0.01	17.28±0.06	$-2.06^{+0.13}_{-0.12}$	0.64±0.09	-	-	-	-
CX Tau	$0.65^{+0.05}_{-0.04}$	$19.22^{+1.57}_{-1.72}$	$11.71^{+3.18}_{-4.74}$	$-3.78^{+1.30}_{-0.90}$	-	-	-	-
CY Tau	0.66±0.02	$15.75^{+0.50}_{-0.49}$	$-5.19^{+1.51}_{-1.56}$	$1.32^{+0.47}_{-0.44}$	-	-	-	-
DN Tau	$0.74^{+0.07}_{-0.03}$	$19.14^{+1.08}_{-1.13}$	$12.57^{+2.29}_{-5.42}$	$-4.28^{+2.09}_{-0.78}$	-	-	-	-
DR Tau	0.37±0.01	$18.38^{+0.08}_{-0.07}$	-1.77±0.09	$0.39^{+0.07}_{-0.06}$	-	-	-	-
FT Tau	0.44±0.01	$16.85^{+0.10}_{-0.11}$	-0.84±0.11	-0.44±0.07	-	-	-	-
RNO 90	0.42±0.01	$17.77^{+0.04}_{-0.05}$	-1.22±0.06	$0.50^{+0.04}_{-0.05}$	-	-	-	-
XX Cha	0.48±0.01	17.33±0.08	-0.79±0.12	-0.26±0.09	-	-	-	-

Table D.4: Fit values for the multiple component fits.

Fixed 4.71 line width								
	BP Tau	CX Tau	CY Tau	DN Tau	DR Tau	FT Tau	RNO 90	XX Cha
T_1	933^{+136}_{-101}	425^{+114}_{-77}	821^{+150}_{-86}	486^{+53}_{-52}	906^{+64}_{-55}	920^{+56}_{-47}	953^{+66}_{-54}	765^{+43}_{-35}
$\log_{10}(N_1)$	18.5±0.2	20.3±1.1	18.7±0.2	$18.7^{+0.5}_{-0.4}$	18.6±0.1	18.5±0.1	18.4±0.1	18.8±0.1
R_1	0.12±0.02	0.13±0.03	$0.08^{+0.02}_{-0.1}$	0.16±0.02	0.39±0.04	0.13±0.01	0.34±0.03	$0.18^{+0.01}_{-0.02}$
T_2	516^{+15}_{-17}	196^{+42}_{-31}	535^{+43}_{-56}	239^{+30}_{-31}	487^{+15}_{-16}	364^{+49}_{-33}	513±13	357^{+55}_{-38}
$\log_{10}(N_2)$	18.2±0.1	$16.3^{+1.1}_{-0.7}$	18.1±0.4	$15.8^{+1.1}_{-0.6}$	18.5±0.1	$18.3^{+0.3}_{-0.2}$	18.2±0.1	18.7±0.2
R_2	0.46±0.02	$4.60^{+3.54}_{-3.19}$	$0.17^{+0.03}_{-0.02}$	$4.21^{+3.37}_{-2.94}$	1.24±0.04	0.44±0.08	1.12±0.05	$0.5^{+0.08}_{-0.07}$
T_3	259^{+18}_{-19}	-	268^{+67}_{-79}	-	247^{+22}_{-23}	217^{+14}_{-15}	295±18	207±12
$\log_{10}(N_3)$	$15.7^{+0.8}_{-0.4}$	-	$15.6^{+0.8}_{-0.5}$	-	$16.7^{+0.5}_{-0.4}$	$16.0^{+0.6}_{-0.4}$	16.4±0.5	$16.3^{+0.6}_{-0.4}$
R_3	$7.59^{+4.98}_{-4.57}$	-	$2.45^{+3.13}_{-1.55}$	-	$8.39^{+4.41}_{-3.65}$	$9.00^{+4.08}_{-4.28}$	$6.97^{+5.22}_{-3.03}$	$8.79^{4.21}_{-4.19}$
Quadrature line widths								
	BP Tau	CX Tau	CY Tau	DN Tau	DR Tau	FT Tau	RNO 90	XX Cha
T_1	959^{+150}_{-107}	415^{+113}_{-75}	836^{+169}_{-100}	481^{+56}_{-52}	921^{+57}_{-43}	903^{+60}_{-46}	940^{+59}_{-48}	767^{+49}_{-38}
$\log_{10}(N_1)$	17.9±0.2	19.7±1.1	$18.0^{+0.3}_{-0.2}$	$18.2^{+0.5}_{-0.4}$	18.1±0.1	17.9±0.1	17.8±0.1	18.2±0.1
R_1	$0.19^{+0.05}_{-0.04}$	0.25±0.06	0.13±0.04	0.30±0.04	$0.68^{+0.05}_{-0.06}$	0.25±0.02	0.62±0.06	$0.31^{+0.03}_{-0.04}$
T_2	517^{+16}_{-17}	192^{+41}_{-28}	530^{+50}_{-65}	231^{+31}_{-32}	491±15	382^{+60}_{-48}	511^{+13}_{-14}	389^{+49}_{-54}
$\log_{10}(N_2)$	17.7±0.1	$16.2^{+0.8}_{-0.6}$	17.7±0.4	$15.8^{+0.8}_{-0.5}$	18.0±0.1	$17.8^{+0.3}_{-0.2}$	17.7±0.1	18.2±0.2
R_2	0.87±0.03	$5.19^{+3.15}_{-2.87}$	$0.30^{+0.04}_{-0.03}$	$4.75^{+3.20}_{-2.72}$	2.34±0.08	$0.74^{+0.17}_{-0.13}$	2.10±0.08	$0.76^{+0.15}_{-0.09}$
T_3	250^{+17}_{-18}	-	278^{+66}_{-82}	-	242^{+19}_{-20}	215^{+13}_{-14}	289^{+16}_{-17}	202±11
$\log_{10}(N_3)$	$15.7^{+0.5}_{-0.3}$	-	$15.7^{+0.8}_{-0.5}$	-	16.5±0.3	$15.9^{+0.4}_{-0.3}$	$16.1^{+0.3}_{-0.2}$	$16.2^{+0.4}_{-0.3}$
R_3	$9.67^{+3.64}_{-3.93}$	-	$2.42^{+3.40}_{-1.50}$	-	$11.8^{+2.21}_{-2.62}$	$10.62^{+3.01}_{-3.48}$	$10.84^{+2.80}_{-2.76}$	$10.60^{+2.98}_{-3.03}$

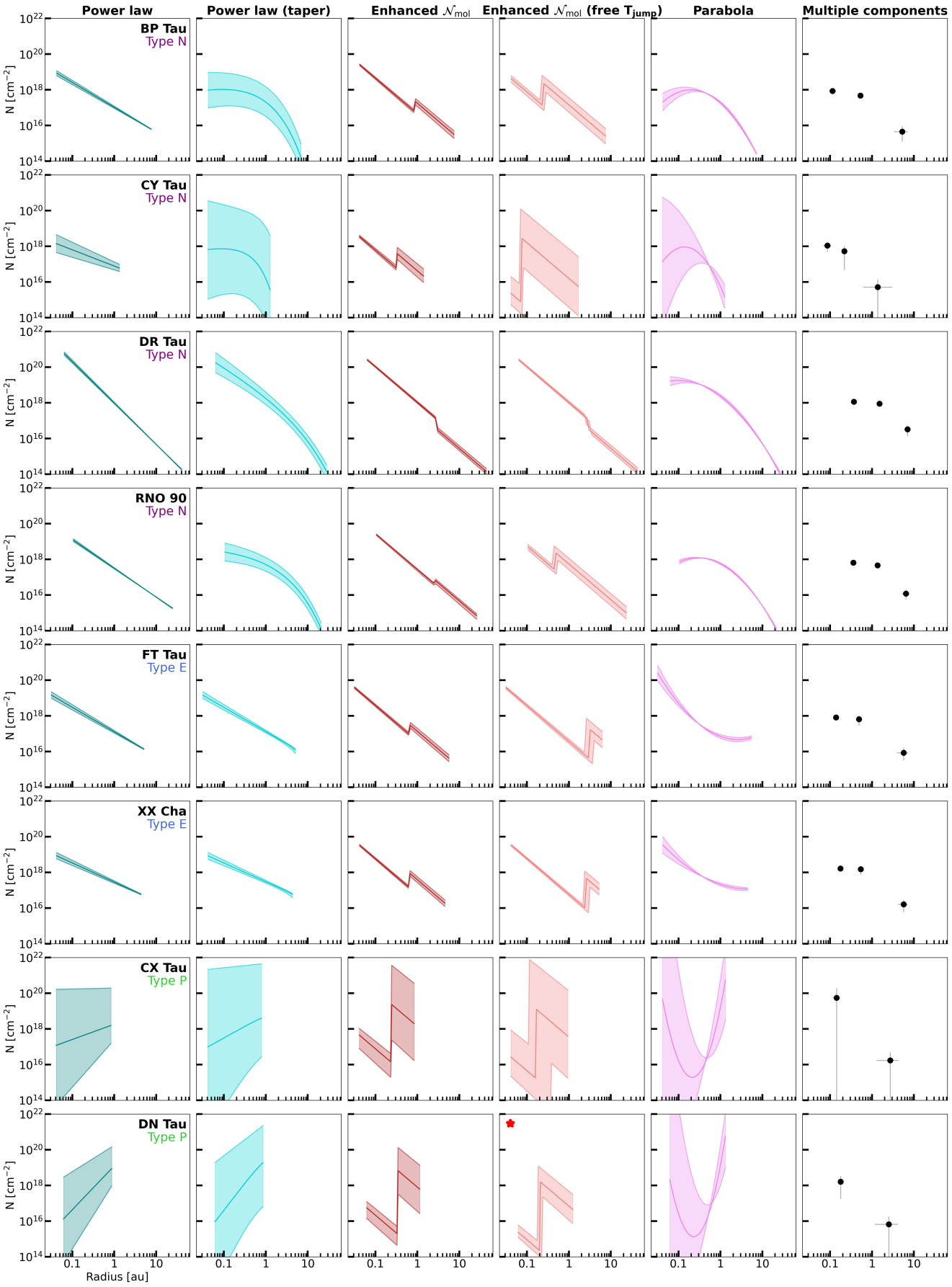

Fig. D.1: Similar to Figure 3, but for the quadrature line widths. The shaded area is the 1σ-confidence interval, given the uncertainties listed in Tables D.3.

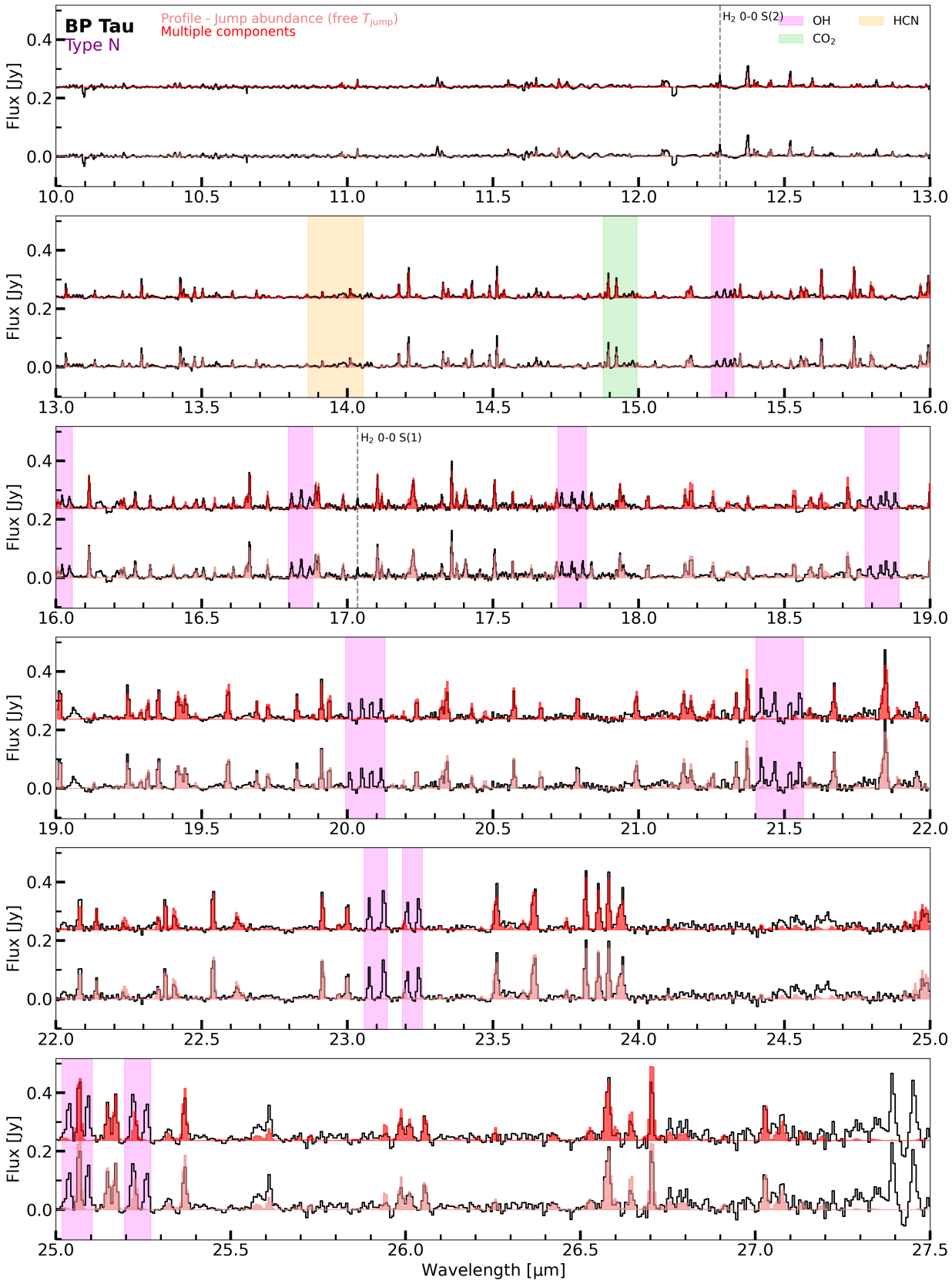

Fig. D.2: Comparison between the full models of the best-fitting parametric model (bottom fit) and of the multiple components (red, top fit) for BP Tau. The colour of the best-fitting profile matches that of Figure 3. Indicated are also the molecular features from OH (magenta), CO_2 (green), and HCN (orange). The vertical lines indicate the S(1) and S(2) transitions of H_2.

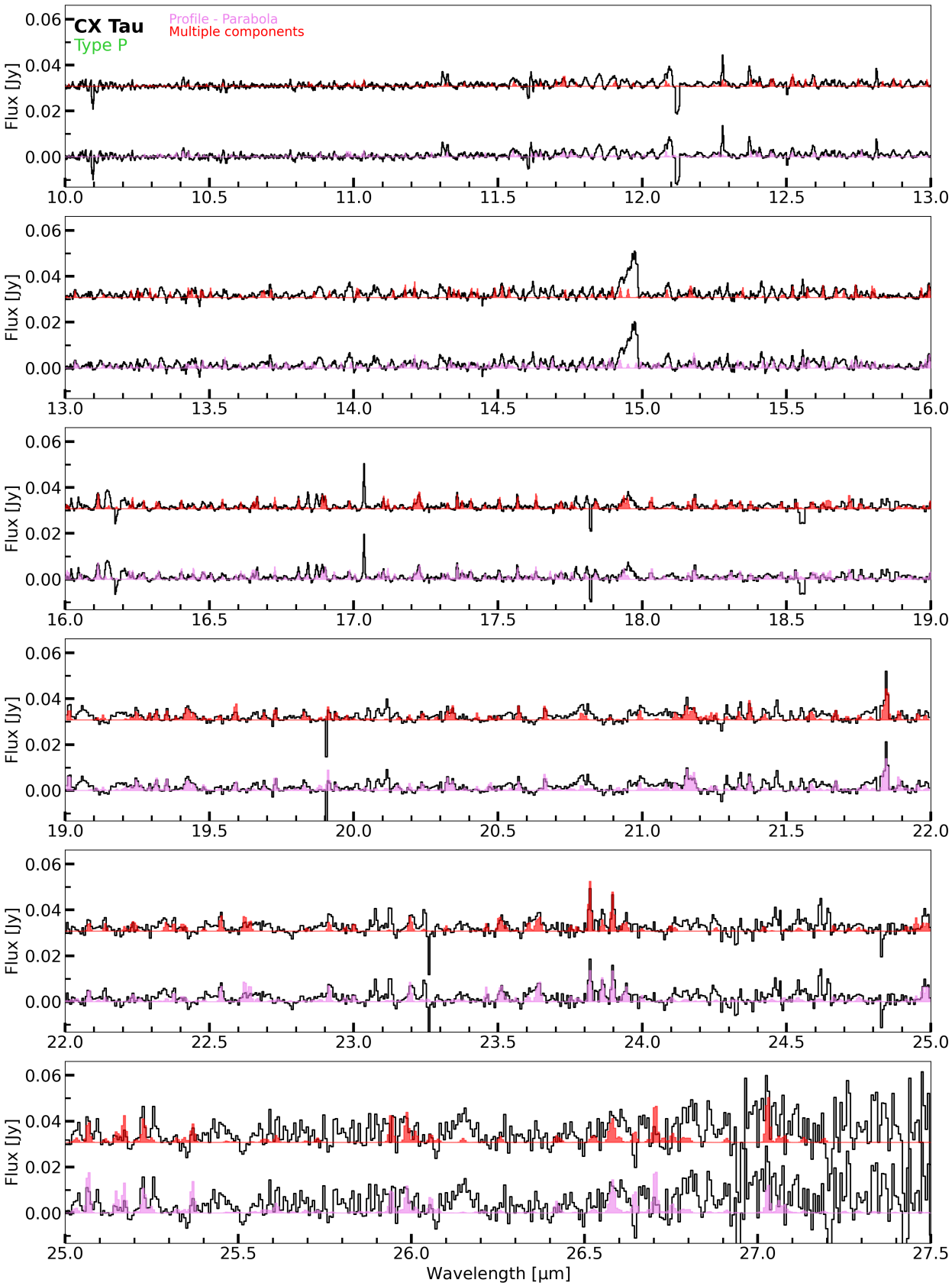

Fig. D.3: Similar as Figure D.2, but for CX Tau. We refer the reader to Vlasblom et al. (2025) for the other molecular emission features.

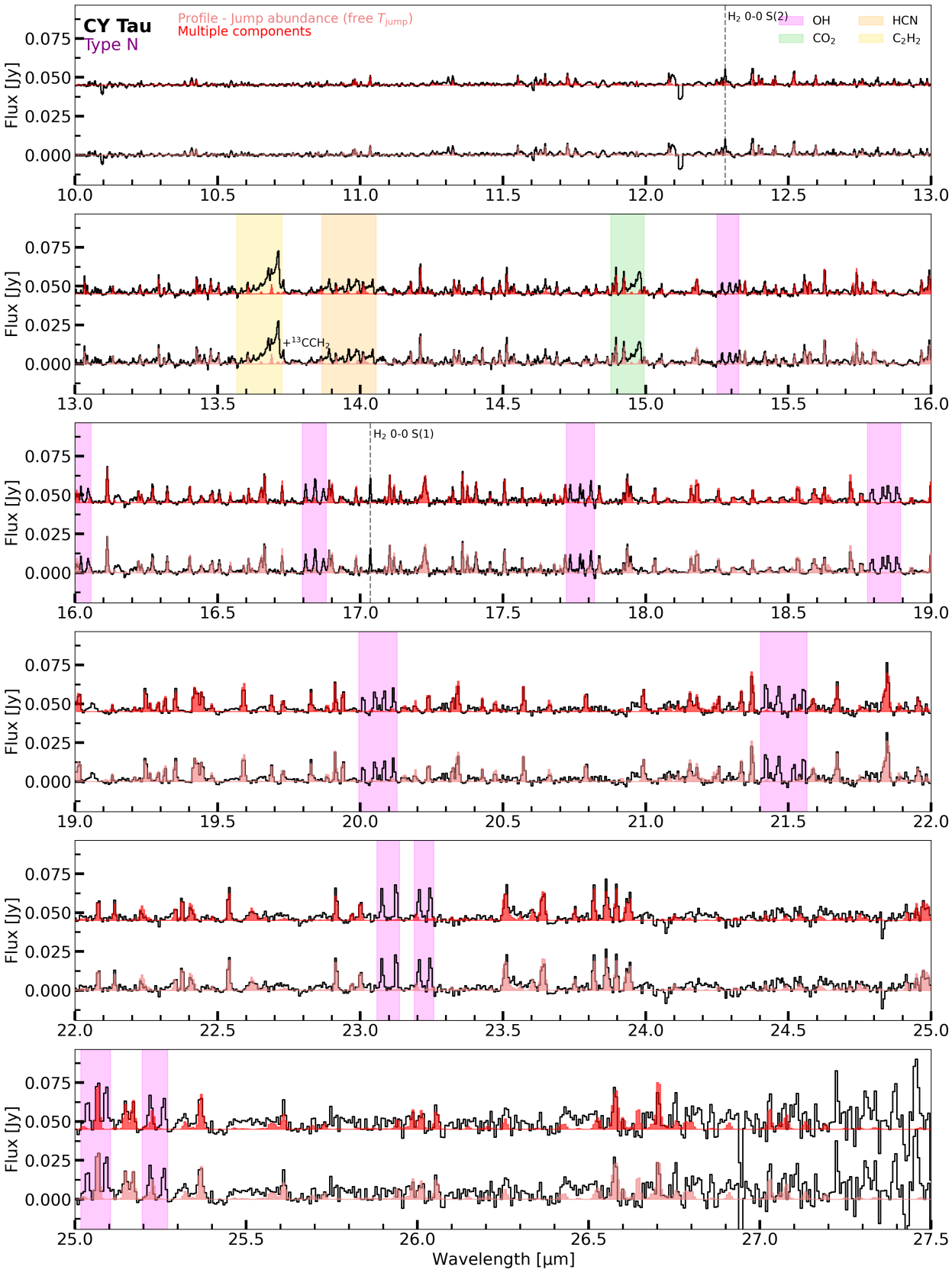

Fig. D.4: Similar as Figure D.2, but for CY Tau. Highlighted in yellow is the C_2H_2 emission feature, while the approximate location of $^{13}CCH_2$ is also shown.

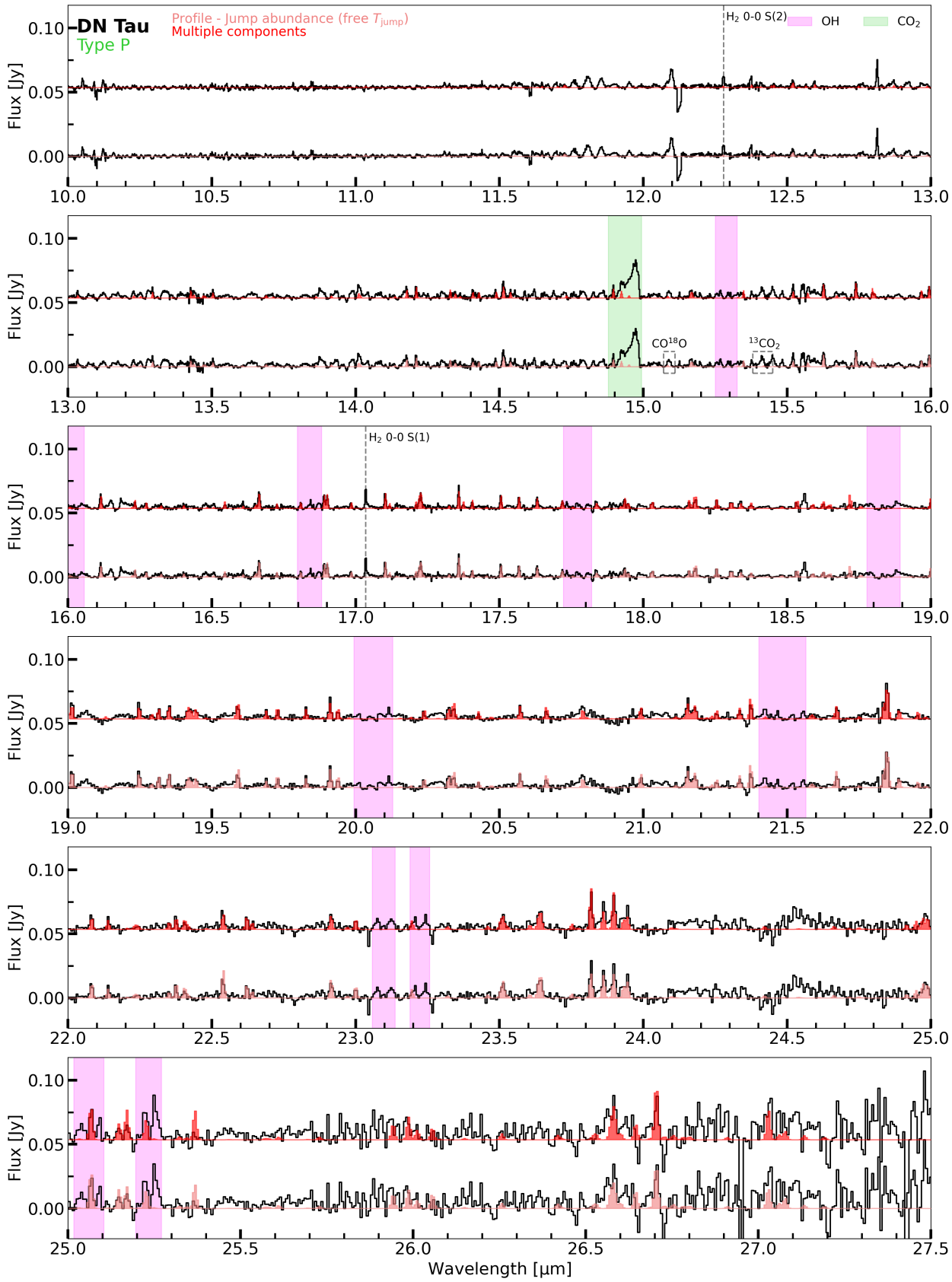

Fig. D.5: Similar as Figure D.2, but for DN Tau. The boxes indicate the detection of $^{13}CO_2$ and the potential detection of $CO^{18}O$.

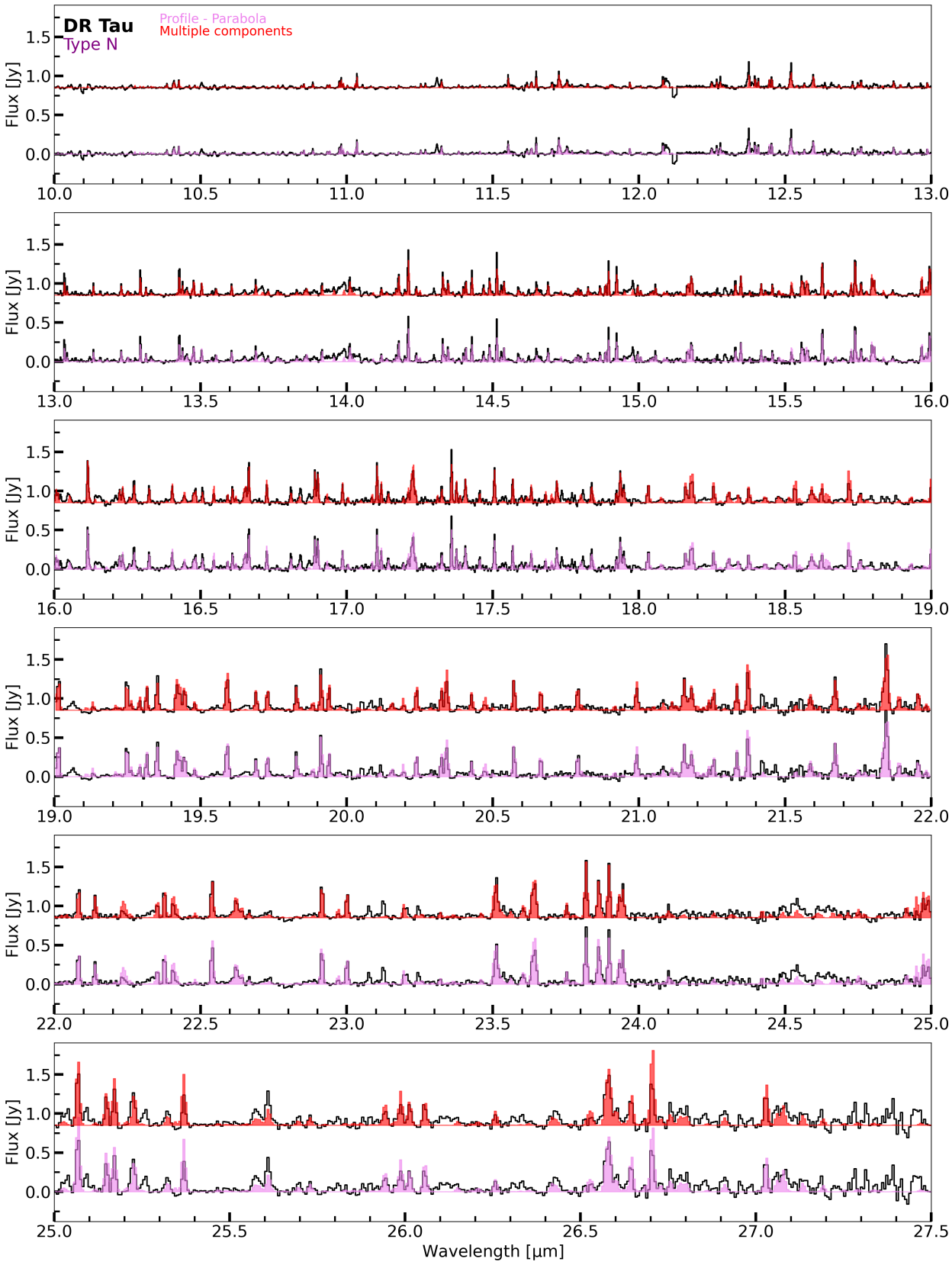

Fig. D.6: Similar as Figure D.2, but for DR Tau. We refer the reader to Temmink et al. (2024b) and Temmink et al. (2024a) for the other molecular emission features.

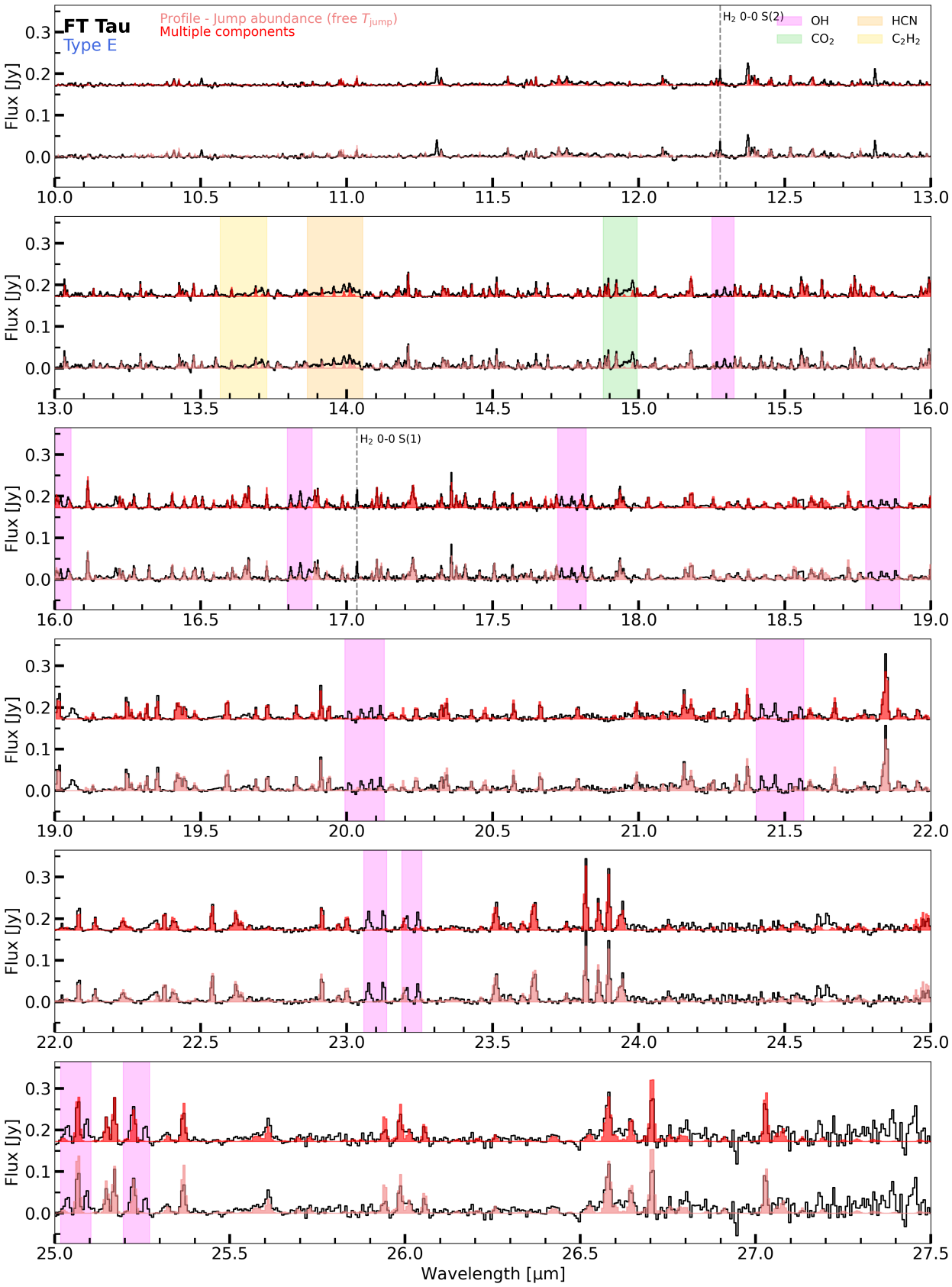

Fig. D.7: Similar as Figure D.2, but for FT Tau. Highlighted in yellow is the C_2H_2 emission feature.

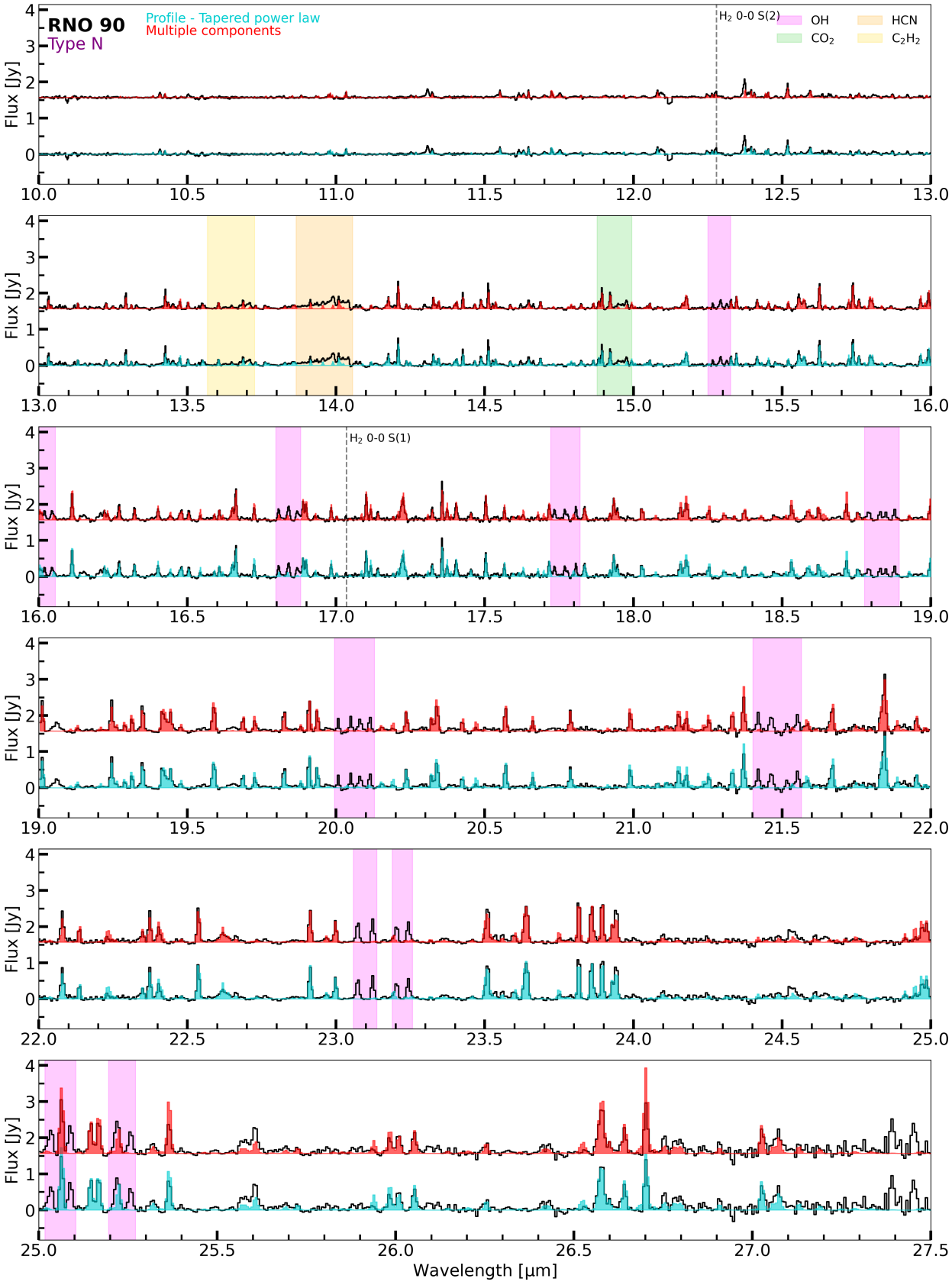

Fig. D.8: Similar as Figure D.2, but for RNO 90. Highlighted in yellow is the C_2H_2 emission feature.

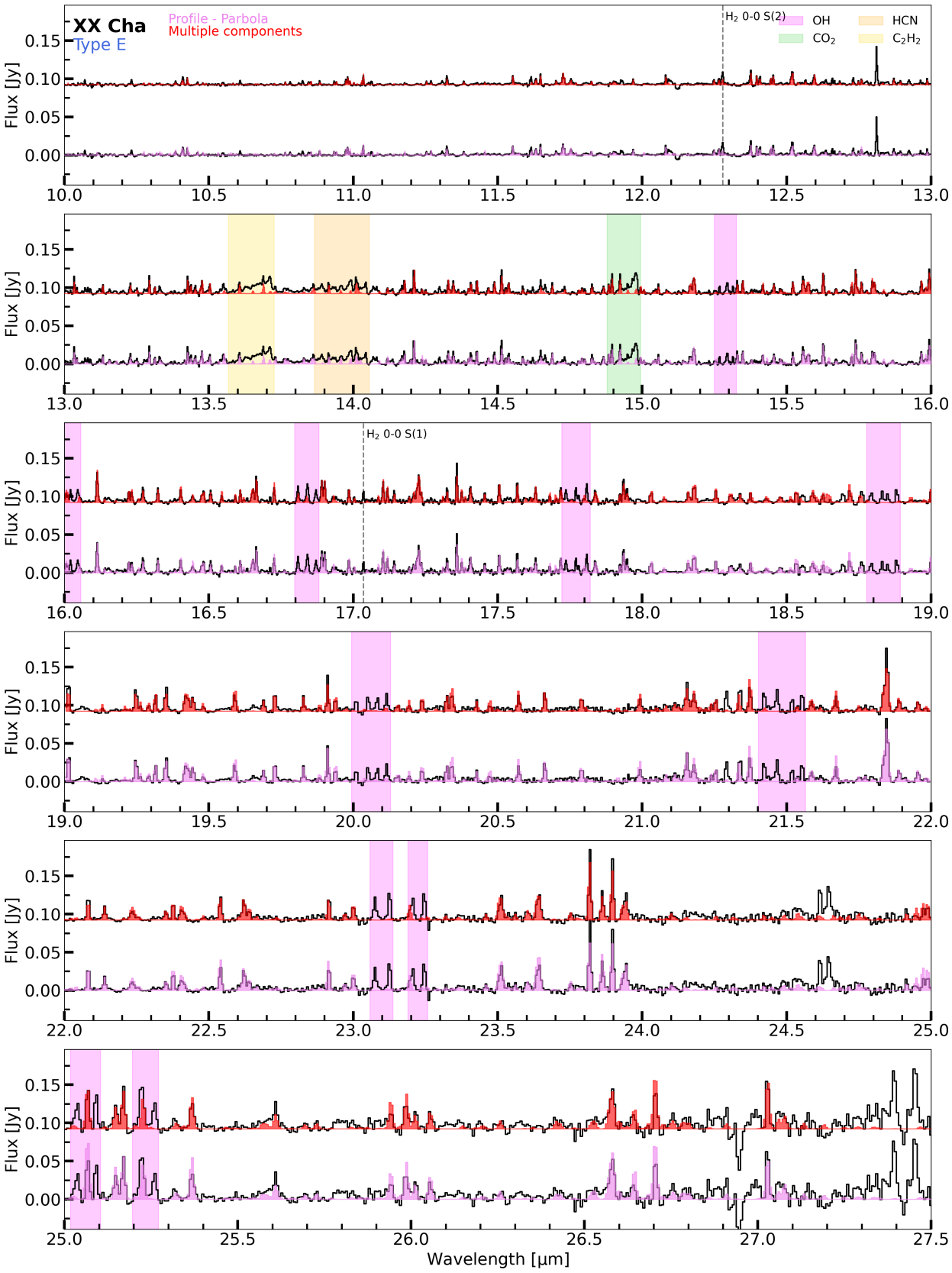

Fig. D.9: Similar as Figure D.2, but for XX Cha. Highlighted in yellow is the C_2H_2 emission feature.

Appendix E: Other molecular species

In this following section, we discuss the observed molecular species, aside from H_2O, in each disk (Section E.1) and we discuss the tentative detection of CH_4 in CY Tau (Sectoin E.2). These features are also highlighted in Figures D.2-D.9.

E.1. Molecules per source

BP Tau: Aside from the pure rotational H_2O lines, the spectrum of BP Tau also contains strong emission of the ro-vibrational transitions and CO emission at the shortest wavelengths (4.9-5.3 μm). Other molecular species, such as CO_2 and HCN, are only weakly detected, while OH transitions are strongly detected above >15 μm. Both the H_2 0-0 S(1) (at 17.30484 μm) and S(2) (at 12.27861 μm) are detected. The detected molecular species at >10 μm are also highlighted in Figure D.2.

CY Tau: The strongest molecular feature in the spectrum of CY Tau belongs to C_2H_2, also visible in Figure 1. Its isotopologue, $^{13}CCH_2$ is also well detected. Other molecular species include CO, the ro-vibrational lines of H_2O, OH, HCN, and CO_2. Both the H_2 S(1) and S(2) transitions are also detected. Additionally, we present a potential detection of CH_4 in this disk. The tentative detection is further highlighted in Section E.2. The molecular species are highlighted in Figure D.4.

DN Tau: DN Tau has previously been classified, just as CX Tau, as a CO_2-rich source (Pontoppidan et al. 2010). Aside from the strong emission of CO_2, we report the detection of its isotopologue $^{13}CO_2$ and the potential detection of $CO^{18}O$. Other molecular species, such as HCN and C_2H_2 are not confidently detected, while OH is. At the shortest wavelengths, CO is only tentatively detected, while emission from the ro-vibrational H_2O transitions is clearly detected. As for the other sources, both the H_2 S(1) and S(2) transitions are also detected. Figure D.5 highlights the detected molecular species.

FT Tau: Aside from the strong pure rotational H_2O emission, the spectrum of FT Tau also contains emission from the ro-vibrational lines and from CO. At the longer wavelengths, we clearly detect OH, CO_2, HCN, and C_2H_2. The H_2 S(1) and S(2) transitions are also detected. The emission of these species is also highlighted in Figure D.7.

RNO 90: Besides the rotational H_2O transitions, the spectrum of RNO 90 also contains emission from CO, the ro-vibrational H_2O transitions, OH, CO_2, HCN, and C_2H_2. Both the S(1) and S(2) transitions of H_2 are also detected. The molecular emission is highlighted in Figure D.8.

XX Cha: Although the spectrum of XX Cha is very similar to that of FT Tau, the emission from both CO_2 and C_2H_2 is stronger. Emission from CO, the ro-vibrational H_2O lines, OH, and HCN are also clearly detected. As for all the other sources, both the H_2 S(1) and S(2) transitions are also detected. Figure D.9 highlights the molecular emission of the other species in the spectrum of XX Cha.

E.2. Tentative detection of CH_4 in CY Tau

We report a tentative detection of CH_4 in the spectrum of CY Tau, whose Q-branch is located at ~7.66 μm. In Figure E.1, we display the 7.60-8.00 μm wavelength region, containing molecular emission from ro-vibrational H_2O transitions and potential weak features from C_2H_2 and the potential detection of CH_4. For the slab models (H_2O, C_2H_2, and CH_4) we have used excitation temperatures of 975 K, 500 K, and 500 K, column densities ($\log_{10}(N)$ with N in cm^{-2}) of 18.4, 17.0, and 16.8, and emitting radii of 0.03 au, 0.10 au, and 0.10 au, respectively. The parameters for H_2O and C_2H_2 were obtained using a $\chi^2_{\rm red}$-approach similar to that described in Section 3.1 but using grids instead of an MCMC exploration (see also, for example, Grant et al. 2023). The model for CH_4 has been obtained by visually fitting the residuals. These slab models thus suggest a column density ratio of $N_{C_2H_2}/N_{CH_4} \gtrsim 1.5$, under the assumption that the species are co-existing. The potential presence of CH_4, in addition to the detection of $^{13}CCH_2$, suggests that CY Tau may be the most carbon-rich disk in our sample. This disk may be similar to the much larger disk of DoAr 33, where Colmenares et al. (2024) reported, alongside other hydrocarbons, a tentative detection of CH_4. They compared their spectra to thermochemical models and argued for an overall carbon-to-oxygen ratio (C/O) larger than unity.

Appendix F: Integrated line fluxes

Table F.1: Integrated fluxes for the lines tracing the cold, intermediate, and hot H_2O reservoirs.

Source	F_{1448K}	F_{1615K}	F_{3646K}	F_{6052K}	F^{α}_{1500K}
BP Tau	10.67±0.07	10.43±0.04	6.68±0.05	3.15±0.05	21.09±0.08
CX Tau	0.99±0.02	0.93±0.02	0.49±0.03	0.09±0.03	1.91±0.03
CY Tau	1.17±0.01	1.22±0.01	1.02±0.01	0.60±0.01	2.40±0.01
DN Tau	1.29±0.03	1.49±0.05	0.57±0.02	0.13±0.02	2.78±0.06
DR Tau	36.38±0.20	33.89±0.16	24.94±3.17	13.49±0.26	70.27±0.26
FT Tau	8.60±0.03	6.99±0.03	2.81±0.03	2.13±0.03	15.59±0.05
RNO 90	66.03±0.26	66.65±0.22	40.82±0.19	24.72±0.27	132.68±0.34
XX Cha	4.23±0.01	3.88±0.02	1.54±0.01	1.09±0.01	8.11±0.02

Notes. The fluxes are given in $\times 10^{-15}$ erg s^{-1} cm^{-2}.
$^{\alpha}$: The F_{1500K} flux is the summation of the fluxes of the 1448 K and 1615 K lines, following Banzatti et al. (2025).

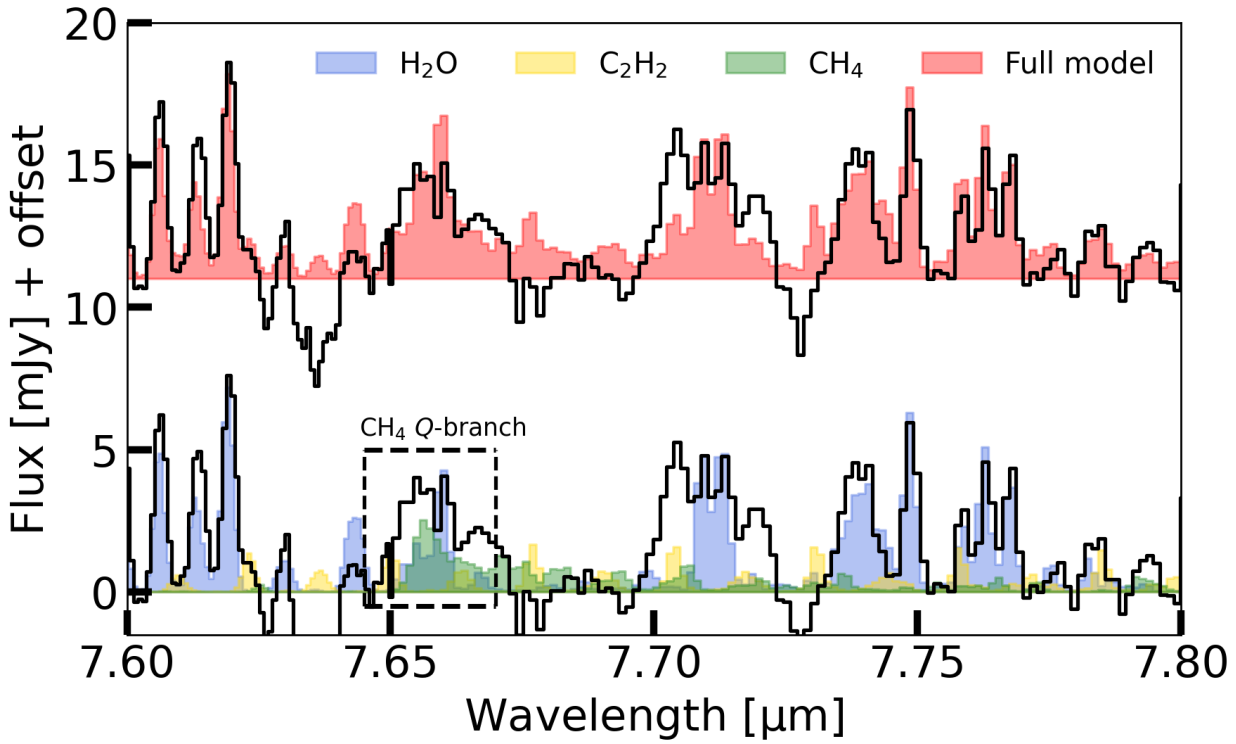

Fig. E.1: Zoom-in on the 7.60-8.00 μm region of CY Tau, showing the potential detection of CH_4 (green). Also shown are approximate contributions from H_2O (blue) and C_2H_2 (yellow) slab models. The full model is shown in red with a small offset applied to the flux.

Appendix G: Profile comparison

In Figures G.1, G.2, and G.3 we show the flux contributions of the 50 slab models for the profiles fitted for DR Tau, CX Tau, and FT Tau, respectively. These disks are each part of one of the different types and comparing their contribution plots provides information on how well the different profiles fit for their types.

DR Tau (Type N): The Type N disks (BP Tau, CY Tau, DR Tau, and RNO 90) are overall best described by the exponentially tapered power laws, the jump abundances with the jump occurring at high temperatures, and upward parabola (see also Table D.1). As can be seen in Figure G.1, those profiles all yield very similar contributions. The main differences between those profiles and the ones with the simple power law or the jump abundance with the jump fixed at $T_{\rm jump}$=400 K is the flux at the shortest wavelengths (<15.0 μm), best probed by the hottest component, where the power law and the fixed temperature jump abundance have stronger contributions of the hotter components (most notable in the left panels of Figure G.1. These stronger contributions results in overfitting the observed flux in those inner regions, whereas the preferred profiles have a decrease in column density in the innermost and, therefore, do not overfit these inner regions.

CX Tau (Type P): The Type P disks (CX Tau and DN Tau) mainly prefer the downward parabola and jump abundance profiles (see also Table D.1). As can be seen in Figure G.2, those profiles have the strongest contributions from either the hot or intermediate and cold components, while the (tapered) power law profiles are not able to capture the strength of all three components (hot, intermediate, and cold). The preference for these profiles shows that the P Type disks do have contributions from at least two of the components.

FT Tau (Type E): FT Tau and XX Cha, the Type E disks, are best described by a jump abundance at low temperatures or a smooth power law (see also Table D.1). As can be seen in Figure G.3 for FT Tau, the jump abundance with a jump at $T_{\rm jump} \lesssim$250 K is really able to capture the strength of the cold component. The power law is not able to capture this cold component as strongly, but the contributions are clearly still there. The parabola, while being able to yield a similar contribution to the cold component as the power law, has a much stronger contribution at the shortest wavelengths (<15.0 μm) following its upward turn. This stronger contribution actually overfits the observed flux at these wavelengths, disfavouring the parabola as the best fit.

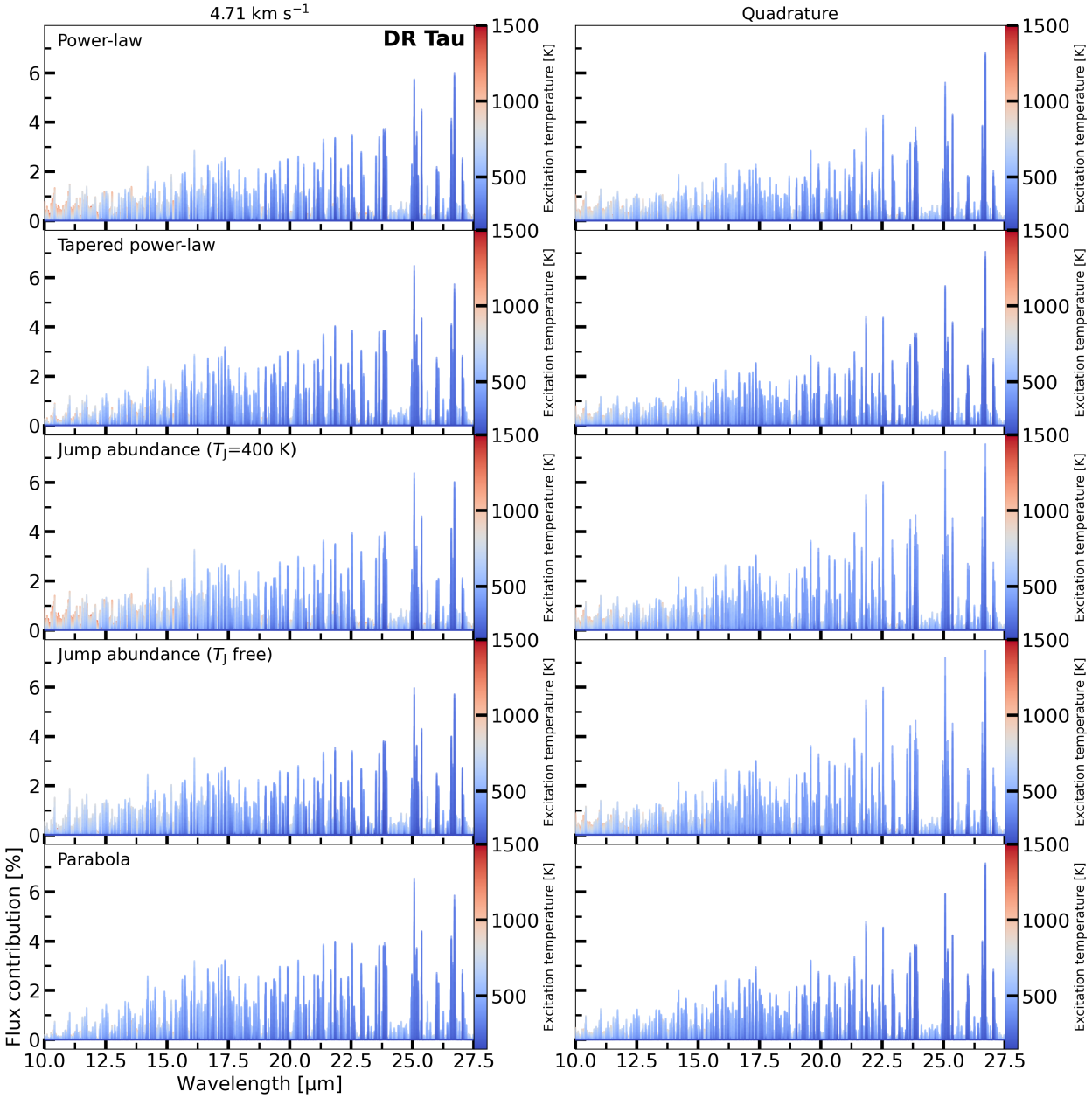

Fig. G.1: The contributions from all parametric fits for DR Tau, representing the Type N disks.

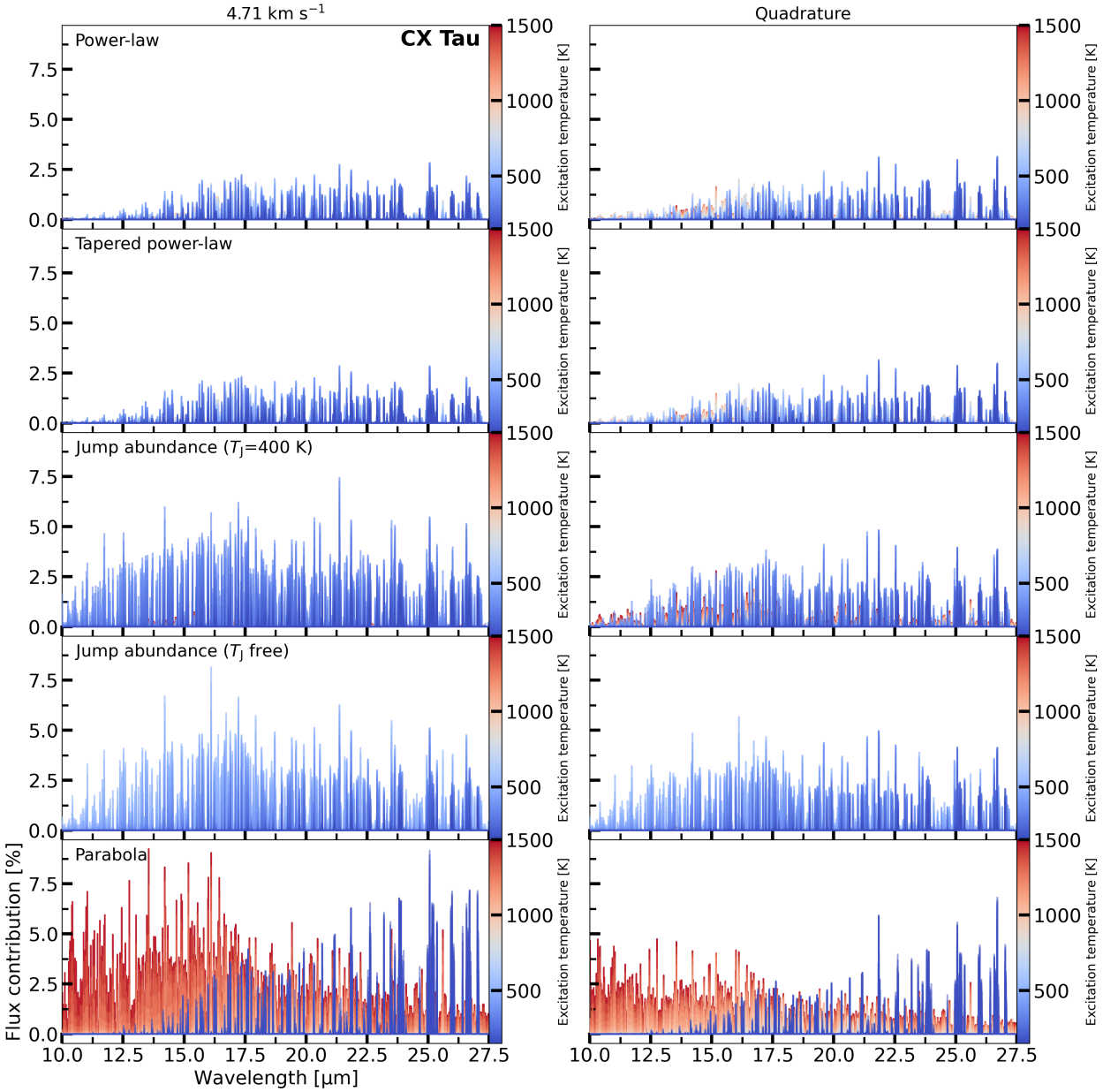

Fig. G.2: Similar as Figure G.1, but for CX Tau, representing the Type P disks.

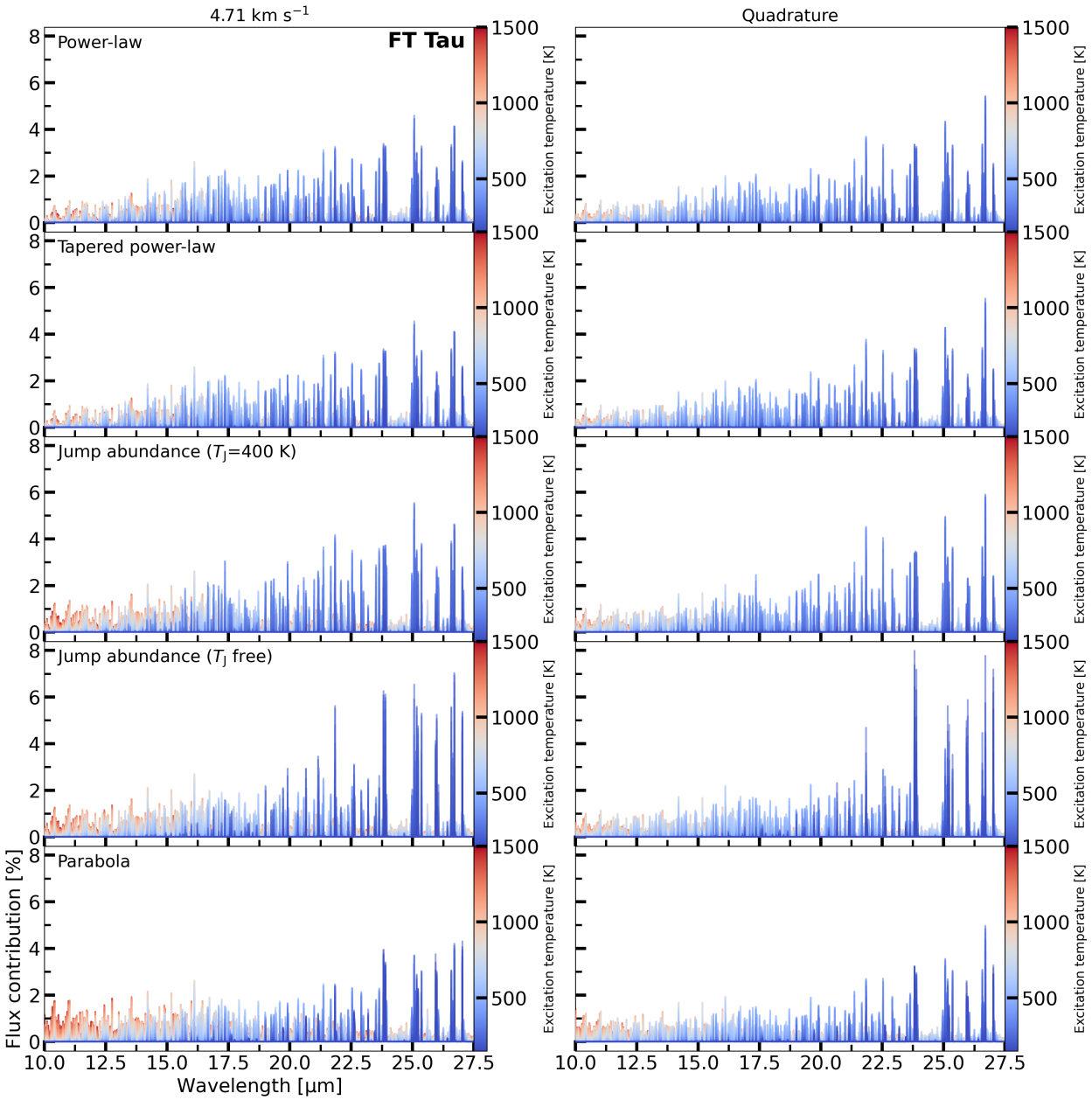

Fig. G.3: Similar as Figure G.1, but for FT Tau, representing the Type E disks.